JGR Oceans

Key Points:
- The location of the Subtropical Front varies on seasonal to decadal time scales with larger meridional shifts away from shallow bathymetry
- Over the Tasman Sea interannual variability is connected to upper ocean heat and freshwater content anomalies, driven by oceanic transports
- These anomalous transports are a consequence of regional wind stress curl anomalies around New Zealand

Correspondence to:
E. Behrens,
erik.behrens@niwa.co.nz

Seasonal and Interannual Variability of the Subtropical Front in the New Zealand Region

Erik Behrens[1] , **Andrew McC. Hogg[2]** , **Matthew H. England[3]** , and **Helen Bostock[4]**

[1]National Institute of Water and Atmospheric Research, Wellington, New Zealand, [2]Research School of Earth Science and ARC Centre of Excellence for Climate Extremes, The Australian National University, Canberra, Australia, [3]Climate Change Research Centre and ARC Centre of Excellence for Climate Extremes, University of New South Wales, Sydney, Australia, [4]School of Earth and Environmental Sciences, The University of Queensland, Brisbane, Australia

Abstract The meridional variability of the Subtropical Front (STF) and the drivers of variability on interannual time scales in the New Zealand region are analyzed using a multi-decadal eddy-resolving ocean hindcast model, in comparison with Argo data. The STF marks the water mass boundary between subtropical waters and subantarctic waters, and is defined as the southern-most location of the 11°C isotherm and 34.8 psu isohaline between 100 and 500 m. The STF shifts up to 650 km (6°) meridionally on seasonal timescales. In addition to seasonal variability, shifts of around 200 km (2°) occur on interannual time scales. These shifts are connected to regional wind stress curl anomalies in the eastern Tasman Sea and east of New Zealand, which trigger Ekman convergence/divergence and Rossby waves and result in meridional transport of heat and salt into/out of the Tasman Sea. The net transports across the northern boundary of the Tasman Sea show the largest sensitivity to these wind stress curl anomalies. During periods of positive wind stress curl anomalies and Ekman convergence, the heat and salt content increases shifting the position of the STF southward. The opposite tendency occurs during periods of negative wind stress curl anomalies. The migration of the STF does not appear to be directly linked to regional climate oscillations.

Plain Language Summary In this study, we investigate how the Subtropical Front around New Zealand varies in space and time. The Subtropical Front is a water mass boundary between subtropical and subantarctic waters and is a region of high biological production due to favorable oceanic conditions (e.g., nutrients and temperature). We observe large seasonal shifts of around 650 km in the open ocean, while reduced near the coast. During summertime the Subtropical Front is located further south than during winter. In addition to the seasonal shifts, interannual variability in the order of 200 km is observed too. Large part of this long-term variability can be linked to heat and salinity changes within the Tasman Sea, mainly driven by changes in regional wind pattern in the eastern Tasman Sea and east of New Zealand.

1. Introduction

The Subtropical Front (STF) defines the boundary between warm, salty subtropical waters and the cold, fresh subantarctic water masses north of the Southern Ocean (Belkin & Gordon, 1996; Deacon, 1982; Orsi et al., 1995; Sokolov & Rintoul, 2009a). The subantarctic Front (SAF) is located to the south of the STF, which marks the northern boundary of the Antarctic Circumpolar Current (ACC). The STF is simple to define, but the environmental conditions controlling the position of the STF are poorly understood. Oceanographic theories propose that the STF should be located at the latitude of zero-wind stress curl, between the subtropical (positive wind stress curl) and the subantarctic (negative wind stress curl) gyre circulation (Munk, 1950). However, the mean position of the STF is around 40°S (Hamilton, 2006), which is 10 degrees north of the zero-wind stress curl which sits at ∼50°S (De Boer et al., 2013). This mismatch between theory and observations has drawn the attention of several modeling studies to improve our understanding of what environmental factors control the position of the STF, and how it may respond to future climate change (De Boer et al., 2013; Graham et al., 2012). However, these studies of the STF have used relatively coarse (1° × 1°) ocean models for example, (Graham et al., 2012; Meijers, 2014), failing to resolve mesoscale processes.

Due to the different water mass properties of the subtropical water and subantarctic water, large differences across the STF of about 4°C–5°C in temperature and 1 psu in salinity occur over distances of ∼200 km (Belkin & Gordon, 1996; Deacon, 1982). As a result the STF has commonly been defined by temperature and salinity criteria and/or their gradient (>1°C/100 km) depending on the specific focus and dataset used in the study (Belkin & Gordon, 1996; Graham & De Boer, 2013; Orsi et al., 1995). However, there have been multiple definitions and criteria, which has further confounded the understanding of the position and width of the STF (e.g., Smith et al., 2013). It has also been found that properties along the STF path evolve and change due to cross-frontal processes and interaction with the bathymetry (Graham et al., 2012).

Using sea surface temperature (SST) gradients from satellite data, it has been found that in deep water regions away from bathymetry, the STF consists of a wide band of fronts, which is referred to as the Subtropical Frontal Zone (STFZ), where the Northern and Southern STF mark its boundary (Graham & De Boer, 2013). In these regions the STF is density compensated with weak flows and therefore it is not possible to define the front based on sea surface height (SSH) (Smith et al., 2013; Sokolov & Rintoul, 2002). However, a range of dynamical approaches have been developed to define the STF as the southern boundary between the subtropical Super Gyre, which connects all three subtropical gyres in the Southern Hemisphere (Cai, 2006), and the ACC (Smythe-Wright et al., 1998; Stramma, 1992). These studies link the STF directly to ocean dynamics, and have led to definitions of a dynamical STF, associated with the western boundary currents of the subtropical gyres (Graham & De Boer, 2013).

In the southwest Pacific, previous work around New Zealand has used hydrographic and satellite data to define the position and the properties of the STF (Belkin & Cornillon, 2003; Butler et al., 1992; Edwards & Emery, 1982; Hamilton, 2006; Jeffrey, 1986; Morris et al., 2001; Smith et al., 2013; Szymanska & Tomczak, 1994; Uddstrom & Oien, 1999). Some of these studies have suffered from distinguishing between local neritic fronts and issues with shallow, complex bathymetry (Chiswell et al., 2015), placing the position of the STF in a wide range of locations, especially in the Tasman Sea and south of New Zealand (Belkin & Cornillon, 2003; Hamilton, 2006; Smith et al., 2013). West of New Zealand, in the deep Tasman Sea, the front is a wide, density-compensated, STFZ delineated by a Northern STF and Southern STF (Hamilton, 2006), while east of New Zealand the STF is narrow and strong and locally known as the Southland Front and constrained by bathymetry (Sutton, 2001), and fits the definition of the dynamical STF forming part of the western boundary current (Chiswell et al., 2015; Graham & De Boer, 2013). Low and medium resolution modeling studies have previously been used to investigate the response of the STF to changes in wind stress curl and the complex bottom topography in this region (Tilburg et al., 2002). Found that the STF east of New Zealand is controlled by topography and westward propagating surface layer thickness gradients.

In this study, we compare the position of the STF on seasonal to interannual scales around New Zealand using Argo hydrographic data and a new high-resolution, eddy-resolving, ocean model for the New Zealand region and South West (SW) Pacific. This resolution is important as the ocean around New Zealand, including the STF region, is dominated by mesoscale eddies on various spatial and temporal scales (Bull et al., 2017; Oke, Pilo, et al., 2019; Oliver et al., 2015, Figure 1). Thus, high-resolution ocean models, that can fully resolve the mesoscale processes, are critical to understanding the dominant processes and variability of the STF in this region.

The paper is organized as follows. Section 2 describes the models which we use for this study, lays out the STF tracking algorithm and introduces the methods (e.g., section and regions) to investigate changes in the location of the STF. Section 3 contains the model validation. Section 4.1 presents the mean location of the STF, and Section 4.2/4.3 the seasonal/interannual variability of the STF. Section 4.4 links the interannual variability of the STF in the Tasman Sea to meridional transport and local wind stress curl. Section 5 provides a discussion and conclusion.

2. Methods

2.1. Model Description

This modeling study is based on output from two forced ocean-sea-ice models, which use NEMO and CICE to simulate the ocean circulation and sea-ice physics respectively. A detailed description of the model setup, known as GO6, can be found in (Storkey et al., 2018). The first model for our study uses the global
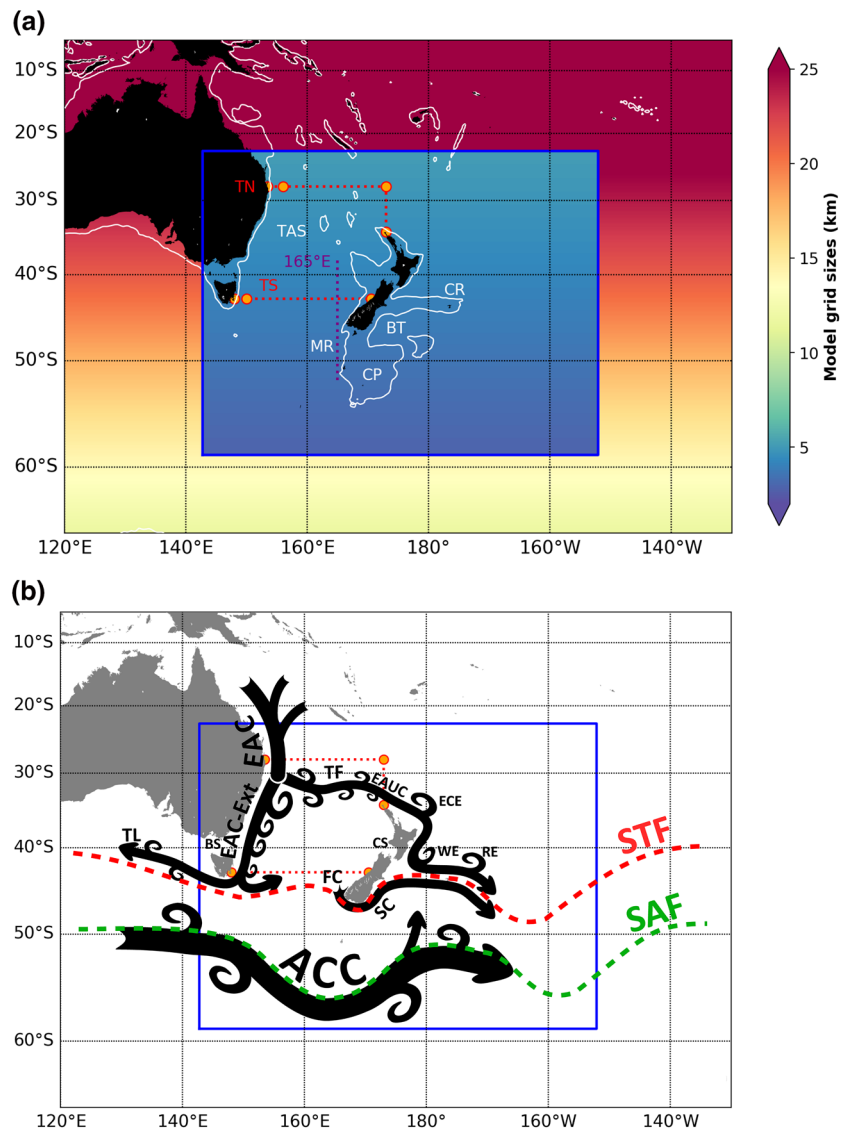
Figure 1. (a) Model grid sizes of the NZ20 configuration in km as colour shading. White contour line shows the 1000m iso-bath. Two sections have been defined to enclose the majority of the Tasman Sea (red dotted), the Tasman North (TN) and Tasman South (TS) section. The orange dots along the sections mark the segments which have been used to calculate transports. A meridional section at 165°E (purple dotted line) has been defined to illustrate the temperature and salinity structure over the water column in the STF region. The Macquarie Ridge (MR), Campbell Plateau (CP), Chatham Rise (CR), Bounty Through (BT), and Tasman Sea (TAS) have been labelled. (b) Schematic of major ocean currents in the region: East Australian Current (EAC), East Australian Current Extension (EAC-Ext), Tasman Front (TF), East Auckland Current (EAUC), Fiordland Current (FC), Southland Current (SC), Antarctic Circumpolar Current (ACC). The Bass Strait (BS), Cook Strait (CS), East Cape Eddy (ECE), Wairarapa Eddy (WE) and Rekohu Eddy (RE) have been labelled. The location of the Subtropical Front (STF) and Subantarctic Front (SAF) has been indicated by the dashed red and green line, respectively.

¼° horizontal eORCA grid of ∼20 km, hereafter eORCA025. eORCA025 is partially mesoscale resolving, also known as eddy-permitting. The second model is identical to eORCA025, but has a high-resolution (1/20°) nested region embedded around New Zealand (Figure 1), in which the grid length is around 4 km, hereafter called NZ20. In this nested region, the model fully resolves mesoscale processes (and partially resolves sub-mesoscale dynamics). The two-way nesting between the global and high-resolution domain is accomplished by AGRIF (Debreu et al., 2008). The high-resolution domain of NZ20 stretches from 142.8°E to 152°W and 59°S to 22°S, with 1304 and 1004 grid cells in x and y direction. Both models use 75-vertical

z-levels in combination with a partial cell approach (Barnier et al., 2006). Layer thickness varies between 1 m at the surface and 200 m in the deep ocean.

In both models a hindcast simulation from 1958–2018 has been performed with atmospheric reanalysis conditions based on JRA-55-DO v1.3 (Tsujino et al., 2018). The simulations have been started from rest with temperature and salinity fields based on an EN4 climatology (Good et al., 2013). A coastal runoff climatology has been applied, and sea surface salinity has been restored to the EN4 climatology with time scales of 30 days for the 1 m depth surface layer. Due to the cold start of both simulations, timeseries in this paper are presented from 1980 onward to allow for potential spin-up effects. Model data has been stored as 5 days means over the simulation period, but the bulk of diagnostics for this paper have been performed using monthly means.

The model output is compared with the Roemmich-Gilson Argo climatology (Roemmich & Gilson, 2009), hereafter referred to as Argo, which provides monthly means for temperature and salinity on a 1° grid for the period from 2004-present. Absolute dynamic topography from satellite has also been used, which is based on a multi-mission altimeter product (Ssalta/Duacs) from Archiving, Validation and Interpretation of Satellite Oceanography data (hereafter referred to as AVISO, Rio & Hernandez, 2004). The AVISO data product covers the period from 1993 to present. Observed values have been compared with the model absolute dynamic topography to evaluate the model and characterize the mean circulation.

2.2. Definition of the STF

In this study we adopted the STF definition of Orsi et al. (1995) with fixed thresholds for temperature (11°C, STF_{TEMP}) and salinity (34.8 psu, STF_{SALT}) and their southernmost location between 100 m and 500 m to identify the STF. The depth range is a slight variation of Orsi et al. (1995), who used the temperature and salinity values at 100 m water depth. This variation was motivated by the subsurface salinity maximum of subtropical waters, which is located deeper than 100 m west of New Zealand and east of the Chatham Rise during autumn (not shown). Consequently, the STF_{SALT} is located up to 1° in latitude further south during that period compared to when salinity at 100 m has been used. The differences between both approaches are not uniform in space and time on interannual timescales. The local differences over the Tasman Sea do not exceed ± 0.2 degrees in latitude but can reach up ± 0.5 degrees latitude east of the Chatham Rise. However, the dominant interannual signals do not appear to be impacted by our choice. Overall, using fixed water mass values below the surface reduces the seasonal variability in the STF (Orsi et al., 1995). The STF based on temperature and salinity is hereafter STF_{TEMP} and STF_{SALT}.

To aid the comparison between data sources with different spatial scales, we apply the most generic and robust criteria (fixed discrete values) to track the STF. We note that the location of the STF depends highly on the selected values for temperature and salinity. Warmer and saltier values will result in a more northerly location of the STF, while cooler and fresher values will yield a more southward position of the STF. Following previous studies, the sensitivity to our choices has been tested by considering variations of ± 1°C and ± 0.2 psu around our selected values to provide a measure of uncertainty (Orsi et al., 1995). Results show a meridional shift between 107 and 278 km for NZ20 (95–277 km for Argo) per 1°C and 56–738 km (1–1420 km for Argo) per 0.2 psu over the region from 1980 to present. The regions with the largest shifts are in the open ocean, with less variation near the coast.

2.3. Control Cross Sections and Regions

We used two control sections to evaluate modeled temperature, salinity and cross section velocity and transports. These control sections enclose a large part of the Tasman Sea (Figure 1; Table 1). The Tasman North section at 28°S, cuts through the East Australian Current (EAC) before the current bifurcates at ~32°S into an eastward extension of the EAC (Oke, Roughan, et al., 2019), historically known as the Tasman Front, and southward flow as part of the EAC Extension (Oliver & Holbrook, 2014). This section allows us to quantify volume transports of EAC and Tasman Front and compare them with previous studies. The Tasman South section at 43°S, runs from Tasmania to the West Coast of New Zealand and characterizes the Tasman Outflow/Tasman Leakage and the net transport through the Tasman Sea. Both sections enclose the central Tasman Sea (labeled TAS) and only neglect the small transports through the Cook Strait (0.7 Sv) and Bass Strait

Table 1
Geographic Coordinates for the Defined Control Cross Sections and Regions shown in Figure 1

Name	Longitudes	Latitudes
Tasman North (TN)	153.5°E, 156°E, 173°E, 173°E	28°S,28°S, 28°S, 34.4°S
Tasman South (TS)	148°E, 150°E, 170.5°E	43°S, 43°S, 43°S
Tasman Sea (TAS)	148°E, 173°E	28°S, 43°S
165°E	165°E	52°S, 38°S

(0.5 Sv). Transports through these shallow passages with water depths less than 300 and 155 m, respectively, are considered too minor to affect large scale variability in the central Tasman Sea. The upper 500 m net transport of heat and freshwater across Tasman North and South sections have been used to compute the contribution to the heat and freshwater content changes, which allows an assessment of the importance of oceanic transports compared to surface fluxes. To compute freshwater a reference salinity of 34.8 psu has been used. In addition to these sections a meridional section along 165°E (marked in Figures 1a and 4), has been used to evaluate temperature and salinity, and to illustrate the location of the STF. Furthermore, two sub-regions in the Tasman Sea (147–173°E, 43–31°S and 160–173°E, 43°–35°S) have also been used to calculate area averages and show the temporal variability of dynamic topography, SST and wind stress curl.

2.4. Transports

Model transport of volume, heat and freshwater have been calculated to compare them against available observational estimates. For heat transport specific heat capacity of 4000 J/kg/°K has been used, while for freshwater $((S_{\text{ref}}{-}S)/S_{\text{ref}})$ a reference salinity (S_{ref}) of 34.8 psu has been applied.

2.5. Lead-Lag Correlations

To test for remotely forced signals on the Tasman Sea over interannual time scales, lead-lag correlations between the upper 500 m heat transport into the Tasman Sea and SST, absolute dynamic topography, and wind stress curl have been performed. A 23-month Hanning filter has been applied to the monthly input fields from 1980 to 2018 to obtain interannual signals. Only positive correlations and lead times up to three years in SST, absolute dynamic topography and wind stress curl have been considered, so that they are in phase with heat transport. The maximum correlation and associated lead time for each grid box has been recorded. Two-sided significance levels (p) have been computed and only correlations with $p < 0.01$ are considered to be significant.

3. Model Evaluation

3.1. Mean Dynamic Topography and Variance

The mean dynamic topography field for AVISO, which provides a good indication for the near surface circulation, is shown in Figure 2a and characterized by a meridional gradient between subtropical water and subantarctic water, with higher values in the subtropics. Tight contour lines south of 50°S show the influence of the strong ACC. The higher values, compared with the broad zonal mean, along the east coast of Australia highlights the EAC and its extension, which is the western boundary current of the South Pacific. On the east coast of the North Island of New Zealand, elevated values indicate the East Auckland Current (EAUC), also part of the western boundary current, and the permanent East Cape Eddy, Wairarapa Eddy and Rekohu Eddy (see also Figure 1b). The contours associated with the SAF and ACC are displaced south by the Campbell Plateau. East of the Campbell Plateau the contours overshoot to the north into the Bounty Trough, before converging at around a latitude of 52°S.

In comparison to AVISO, eORCA025 presents a positive bias in the subtropics, while parts of the subantarctic show negative biases (Figure 2b). The positive bias is in the order of 5 cm in the Tasman Sea and north of New Zealand, but exceed 10 cm in the EAC Extension, EAUC region, Tasman Front and near Fiordland. As
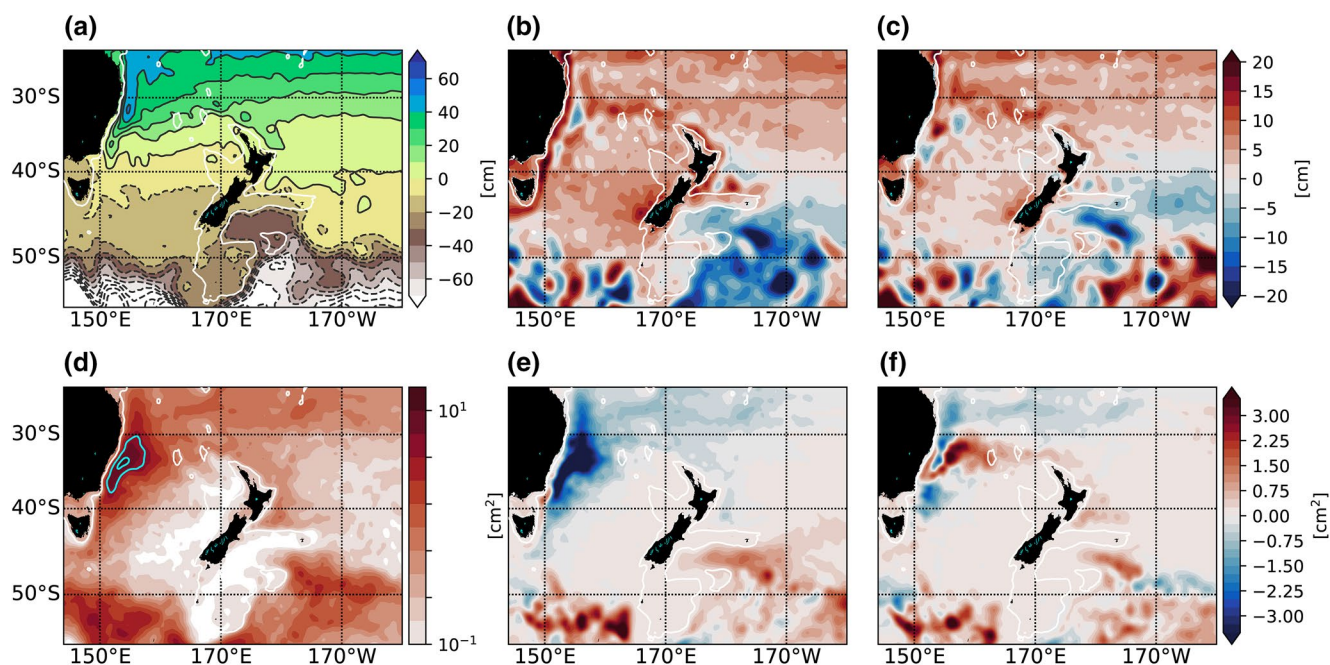
Figure 2. (a) Time mean (1993–2018) dynamic topography from AVISO and biases for (b) eORCA025 and (c) NZ20 in cm. (d) Dynamic topography variance from AVISO and biases for (e) eORCA025 and (f) NZ20 in cm². Contour interval is 10 cm in (a) and 5cm² in (d). The area-average in (a-c) over the region is set to zero to obtain a common reference between AVISO and both models.

a consequence, the increased cross shelf gradient in the EAC Extension, EAUC and over the Chatham Rise suggest stronger near surface oceanic flow than in the observations. To the east of the Campbell Plateau a negative bias, in the order of -5 to -10 cm, is present, while the remaining subantarctic region shows a dipole pattern due to intrinsic eddy variability in the model. NZ20 (Figure 2c) also exhibits a positive bias in the subtropics, but they are smaller than eORCA025 in the Tasman Sea and around New Zealand. In addition, the negative biases east of Campbell Plateau are reduced. The smaller biases in NZ20 in the EAC Extension region and in the boundary current around New Zealand suggest a better alignment of the ocean circulation in the NZ20 model with observations than the eORCA025 model.

Some of this improvement in NZ20 is related to differences in resolution between both models and the ability of NZ20 to capture small scale processes like eddies in key regions (Figures 2d-2f). High eddy variability, as diagnosed from dynamic topography variance, is present in AVISO in the EAC region, where the EAC bifurcates (Oke, Roughan, et al., 2019) (Figure 2d). Elevated eddy activity also occurs in the Tasman Front, which consist of a series of semi-permanent eddies caused by the interaction of the flow with the north-south bathymetry (Oke, Pilo et al., 2019; Oke, Roughan, et al., 2019), along the northeast of New Zealand with the semi-permanent eddies off the East Cape and Wairarapa (Chiswell et al., 2015) and in the ACC (Hogg et al., 2015). eORCA025 (Figure 2e) underestimates eddy variability in particular in the EAC region, shown by large (<-2 cm²) negative bias. We infer that the EAC, EAC Extension and EAUC are too stable and too strong in the eORCA025 model. Higher levels of eddy variability are also present in the ACC and south and east of the Chatham Rise in eORCA025, compared to observations. In NZ20 (Figure 2f) eddy variability in the EAC and EAC Extension region agrees better with AVISO. However, NZ20 overestimates eddy activity in the Tasman Front and along the northeast shelf of the North Island of New Zealand. The bias pattern in NZ20 in the subantarctic is similar to eORCA025, but with slightly smaller positive biases south and east of the Chatham Rise.

3.2. Mean Temperature and Salinity Properties Over the Tasman Sea

In the following, we compare the mean temperature and salinity profile over the Tasman Sea for both models against Argo (Figure 3). This diagnostic helps to identify model biases, which influence our STF
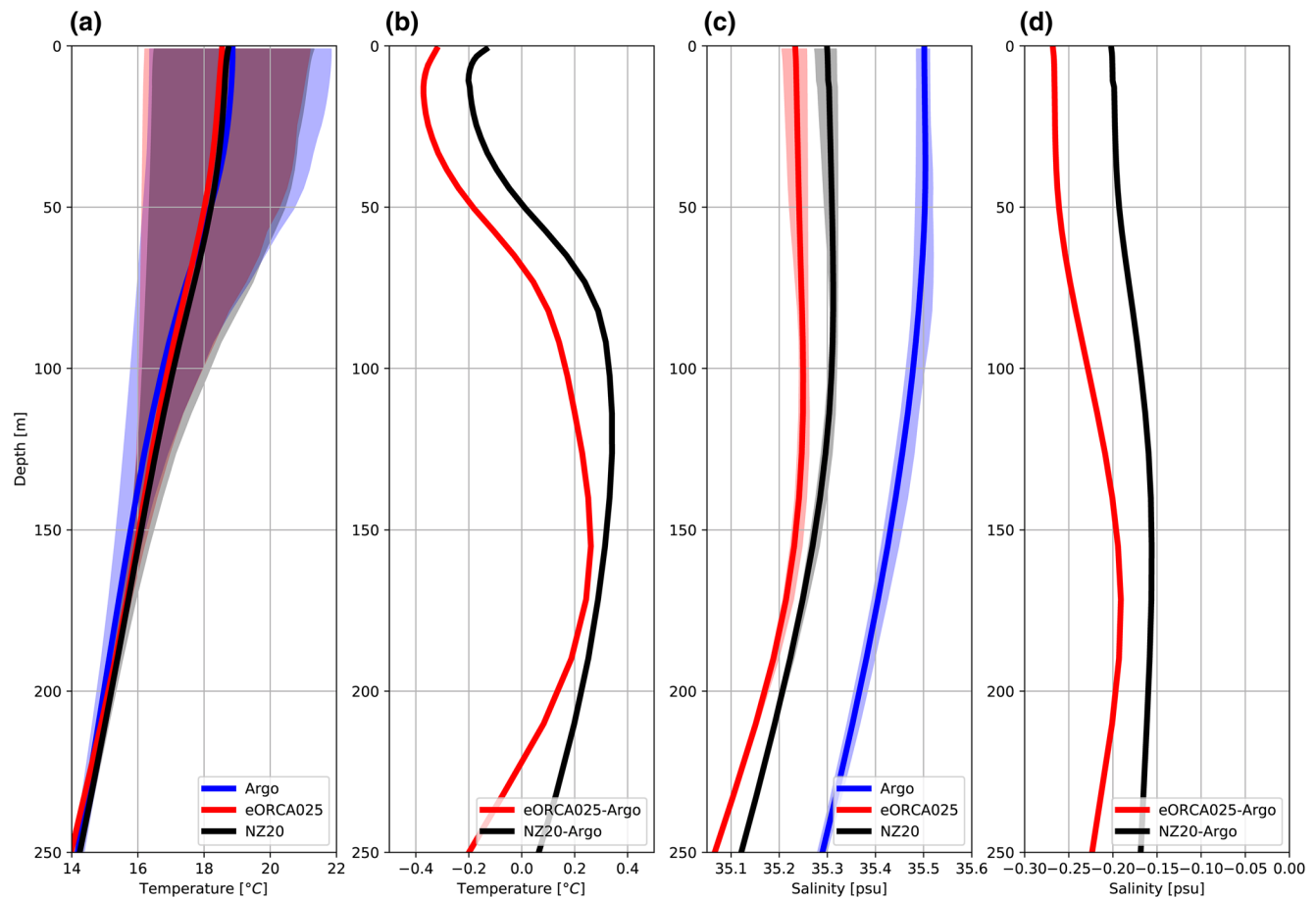
Figure 3. Time averaged temperature (a) and salinity (c) profile over the Tasman Sea region (Figure 1a and Table 1) are presented as solid lines for Argo, eORCA025 and NZ20 for the period from 2004 to 2018. The range is shown by the colour shading. Bias relative to Argo for temperature and salinity are shown in (b) and (d).

detection based on temperature and salinity values. The STF is located south of this region, but model biases in this region in combination with ocean advection will impact the STF detection and hence the location of the STF. For example, when negative salinity anomalies, as a consequence of a fresh salinity bias, are advected by oceanic currents southward then the STF detection would place the STF erroneously further north. In addition, this region will also be used to evaluate freshwater and heat content changes, presented in Section 4.4.

For temperature there is general agreement between both models and Argo in terms of mean temperature and range (Figure 3a). However, both models are up to 0.4°C (eORCA025)/0.2°C (NZ20) too cold in the upper 50 m (Figure 3b) and underestimate the upper limit of the seasonal range by around 0.7°C. Between 100 and 200 m, the temperature bias is around +0.2–0.35°C, but turns negative (cooler) around 220–250 m.

Both models underestimate the salinity compared with Argo salinity data. Here, eORCA025 is around 0.3 psu too fresh, while the bias in NZ20 is reduced to 0.2 psu (Figures 3c and 3d). The Argo profiles show a monotonic freshening with depth, while both models present a local salinity maximum between 70 and 150 m. Despite this general fresh bias, the modeled salinity range (±0.025 psu) is generally comparable to Argo (±0.02 psu).

3.3. Upper 200 m Model Biases

In this section, we investigate the spatial pattern of the average temperature and salinity biases from the models compared with Argo data for the upper 200 m (Figure 4). eORCA025 exhibits a large (>1°C) warm
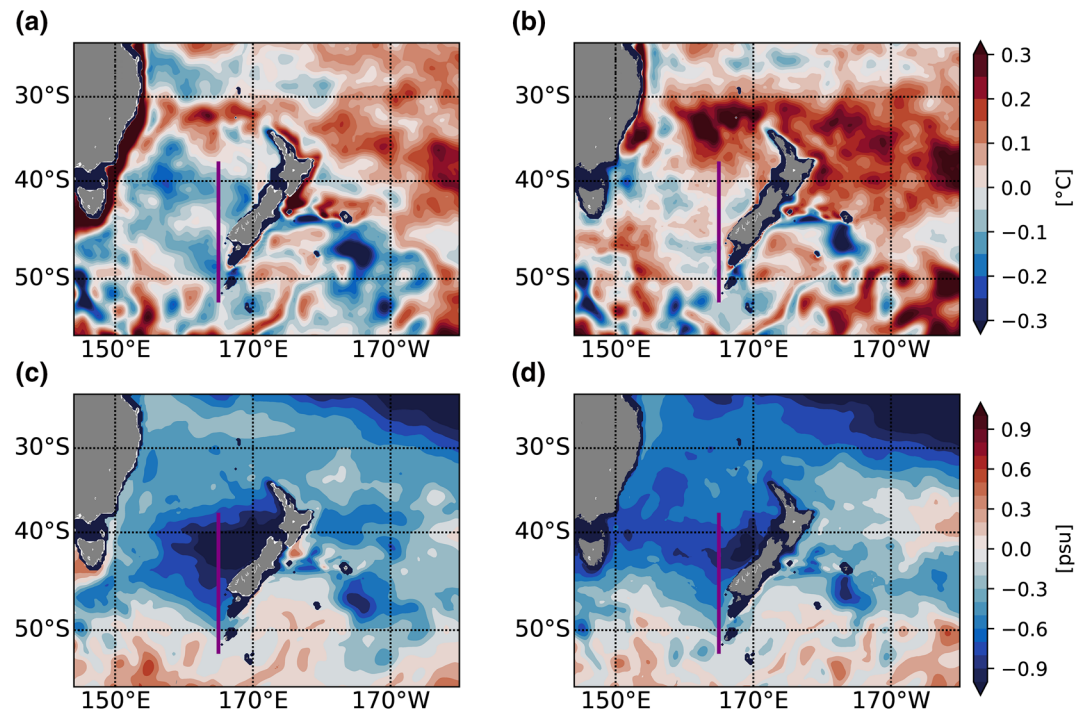
Figure 4. Upper 200m temperature (a-b) and salt (c-d) bias of eORCA025 (left panels) and NZ20 (right panels) against Argo over the period from 2004 to 2018. The purple line (165°E) marks the section used to investigate the impact of model biases on the STF detection (Figure 7).

bias along the entire east coast of Australia. This bias can be attributed to the EAC Extension, which is too stable in eORCA025 (Figure 2e) carrying too much heat southward, rather than transporting this heat into the central Tasman Sea. The consequence is a cold bias (∼−0.5°C) over most of the Tasman Sea in eORCA025. The Tasman Front, the EAUC and its continuation along the east coast of the New Zealand's North Island and Chatham Rise, are characterized by a positive temperature bias in the order of about 0.5°C in both models. This warm bias is a consequence of an excessive heat transport of the Tasman Front in both models. In NZ20 this warm bias around the North Island of New Zealand is enhanced, and exceeds 0.6°C. However, there is no warm bias in the EAC Extension for NZ20. In addition, the Tasman Sea has turned from a cold bias in eORCA025 to a slight warm bias in NZ20, which can be attributed to stronger transport of heat from EAC into the Tasman Sea in NZ20 (Table 2). The overall temperature bias does not show a clear separation between subtropical and subantarctic waters as is seen in salinity.

As shown in Figure 3, both models experience a large-scale fresh bias in the Tasman Sea, which extends further north into the subtropics. In particular, the eastern Tasman Sea is too fresh (>−0.3 psu) in eORCA025 (Figure 4c), while the bias is more widely distributed over the Tasman Sea in NZ20. In contrast to the subtropical region, the subantarctic region, south of 50°S, is characterized by a weak positive salinity bias in both models. Other models with the same atmospheric forcing also exhibits a warm bias around the North Island of New Zealand and a fresh bias in the Tasman Sea for simulations with similar horizontal resolution (Kiss et al., 2020).

As a consequence of the mesoscale eddies in NZ20, the transport of heat in eORCA025 and NZ20 differs, contributing to variations in the biases. The heat transport associated with the EAC is around 15% larger in NZ20 (Table 2). On the other hand, eORCA025 carries around 10% more heat in the EAC Extension to the south than NZ20, while NZ20 transports 4% more heat to the east in the Tasman Front. These numbers reflect differing heat pathways between NZ20 and eORCA025. The larger heat transport of the EAC and Tasman Front in NZ20 compared with eORCA025 contribute to the larger warm biases around the North Island of New Zealand in NZ20. Despite this enhanced bias in NZ20, the bias in the STF region is smaller; in particular, the cold bias over the Tasman Sea is reduced, which leads to a better representation of the STF

Table 2
Time Mean Model Transports (1980–2018) and Observational Estimates for Tasman North Section, Tasman South Section, East Australian Current (EAC), Tasman Front, Middle Section Tasman North and East Australian Current Extension

	Volume (Sv)	Heat transport (PW) (1 PW = 10^{15} W)	Freshwater transport (Sv)
Tasman North eORCA025	−6.3 ± 4.3	−0.3184 ± 0.2	−0.061 ± 0.03
Tasman North NZ20	−6.1 ± 4.2	−0.3059 ± 0.2	−0.058 ± 0.04
Tasman South eORCA025	−5.8 ± 4.2	−0.1964 ± 0.1	−0.023 ± 0.02
Tasman South NZ20	−5.7 ± 4.1	−0.1731 ± 0.1	−0.029 ± 0.02
EAC Observation	−25 to −37 Sv (Ridgway & Dunn, 2003), −22 (Mata et al., 2000), −22 (Sloyan et al., 2016)	–	–
EAC eORCA025	−19.3 ± 7.9	−1.2593 ± 0.4	0.145 ± 0.06
EAC NZ20	−19.8 ± 12.3	−1.4868 ± 0.5	0.197 ± 0.08
Tasman Front Observation	13 Sv (Ridgway & Dunn, 2003), 8 (Stanton, 2010)	–	–
Tasman Front eORCA025	11.3 ± 4.3	0.6218 ± 0.1	−0.10 ± 0.02
Tasman Front NZ20	9.7 ± 5.4	0.644 ± 0.2	−0.13 ± 0.02
Middle section Tasman North eORCA025	1.6 ± 7.9	0.319 ± 0.3	−0.09 ± 0.05
Middle section Tasman North NZ20	3.9 ± 12.9	0.536 ± 0.5	−0.11 ± 0.07
EAC Extension Observation (34°S)	−19 Sv (Ridgway & Dunn, 2003)	–	–
EAC Extension Observation (43°S)	−8.1 to −9.7 (Oliver & Holbrook, 2014)	–	–
EAC Extension eORCA025	−9.4 ± 3.9	−0.3245 ± 0.1	−0.051 ± 0.01
EAC Extension NZ20	−8.6 ± 10.8	−0.2931 ± 0.3	−0.047 ± 0.03

Notes. The modeled transports for EAC, Tasman Front, and Middle section Tasman North are obtained by integrating transports across subsections of the Tasman North section. The modeled transports for EAC, Middle section Tasman North and Tasman Front transports are computed between 153.5°–155.7°E, 155.7°–173°E and 28°–34.4°S, respectively. The modeled EAC Extension transports are computed between 148° and 150°E along the Tasman South sections. These definitions follow previous modeling studies (Behrens et al., 2020; Oliver & Holbrook, 2014). Standard deviations for the modeled transports are provided.

location in NZ20 (see Section 4.1). This improvement is the result of larger heat transport into the Tasman Sea in NZ20, when comparing net heat transport across Tasman North and South sections (see section below).

3.4. Control Sections

The following paragraph describes the model performance along three control sections within the high-resolution domain. The first two sections enclose the Tasman Sea (Tasman North and South sections) and are used to compare the transport of heat and freshwater into the Tasman Sea, which will be later linked to variability in the STF. The third section, a meridional section at 165°E across the STF where the biases are largest, is used to illustrate the location of the STF and assess the model performance against Argo.

3.4.1. Tasman North Section

The mean (2004–2018) temperature, salinity and cross section velocity for Argo along the Tasman North section is shown in Figures 5a, 5d, and 5g. The warmest temperatures (>24°C) are found within the top 50 m close to the Australian Shelf (154°E). Below 100 m the warmest temperatures at each depth are found away from the Australian coast (~155°E), which is also visible in the 11°C isotherm (black line). Along the meridional part of this section (to the right-hand side of the gray dashed line) the temperature declines more rapidly approaching the northern tip of New Zealand, in comparison to the zonal section (left hand side of the gray dashed line). The temperature bias in eORCA025 (Figure 5b) shows a positive bias (~1°C) in the top 500 m between 153°E and 155°E, which is part of the EAC. In addition, a positive bias of around 0.5°C are present in the depth range between 100 and 400 m along the entire section, while the top 100 m are colder (~−0.2°C) than Argo. A negative temperature bias below 400 m exceed −1°C near the coast of Aus-
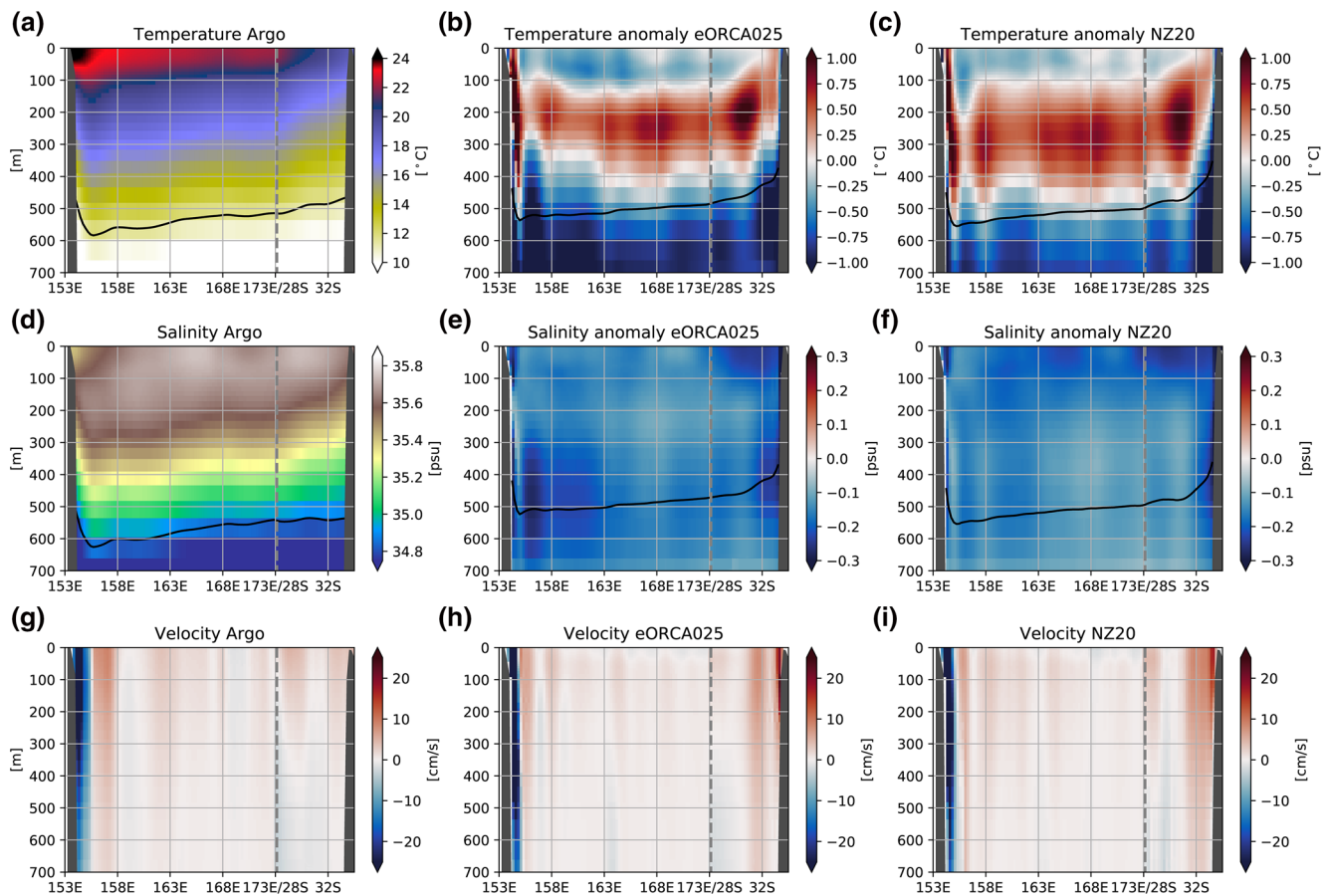
Figure 5. Time mean (2004–2018) observed (a) temperature, (d) salinity, (g) cross-section velocity along the Tasman North section from Argo. The cross section-velocities in Argo are based on the geostrophic flow with level of no motion at 2000m. Biases in temperature and salinity to Argo for (b, e) eORCA025 and (c, f) NZ20, respectively. Modelled cross-section velocities for (h) eORCA025 and (i) NZ20 are shown in comparison to Argo. Northward or eastward velocities have a positive sign. The Tasman North section starts at the Australian coast (153°E) and ends at the northern tip of New Zealand (34°S). Black contour shows the 11°C and 34.8 psu contour, respectively. The dashed line marks where the zonal section turns to a meridional section.

tralia and New Zealand. NZ20 presents a very similar temperature bias pattern (Figure 5c) to eORCA025. The temperatures across the Tasman North section are slightly higher than in eORCA025, which reduces the negative bias in the near surface, but enhances the positive bias. The shape of the 11° isotherm in both models is similar to Argo, with warmer temperature slightly away from the coast and a larger decline in temperatures along the meridional section. Some of the differences seen between Argo and the models within the EAC region are related to an under sampling of Argo in this region, while both models resolve the EAC.

The mean salinity structure from Argo is shown in Figure 5d. The pattern is similar to temperature apart from the lower salinities in the top 100 m near the Australian coast where temperatures are highest. The 34.8 psu isohaline (black line) does not show any differences to the 11° isotherm in Figure 5a. Both models display coherent negative biases of about 0.1 psu over the entire section, with small spatial variations. Reasons for these negative biases remain unknown, but appear to be connected dynamically to the large negative bias seen in the tropical regions (Figures 4c and 4d).

The mean geostrophic velocity from Argo are presented in Figure 5d, with a level of no motion set to 2000 m. The inflow of the EAC is clearly visible by the negative velocities near the Australian coast. A northward recirculation is adjacent to it. The remaining section is characterized by small positive velocities. Both models show a much narrower EAC, which is more focused toward the Australian coast, including the associated recirculations. In the remaining section, models and observation are similar, except for the intensification near New Zealand related to the EAUC. However, other observational data sets (CSIRO Atlas

of Regional Seas) show a similar intensification near New Zealand with zonal velocities exceeding 6 cm/s (see Figures 8d in Ridgway & Dunn, 2003).

Mean transports of volume, heat and freshwater are in the range of observed estimates and other modeling studies (Table 2). The net volume transport across the Tasman North section is −6.3 Sv and −6.1 Sv in eORCA025 and NZ20, respectively; and the net heat transport is calculated to be −0.318 to −0.305 PW (1 PW = 10^{15} W). Thus, southward heat transport through the Tasman Sea in eORCA025 is stronger despite NZ20 showing a larger heat transport in the EAC. These differences suggest that the stronger EAC heat transport in NZ20 is overcompensated for by the enhanced recirculation east of the EAC and the Tasman Front back to the Pacific Ocean, which leads to a lower net heat transport in NZ20 compared to eORCA025 through the Tasman North section. We note a low standard deviation for the EAC Extension volume transport in eORCA025 compared to NZ20, which suggest a more stable boundary current in eORCA025.
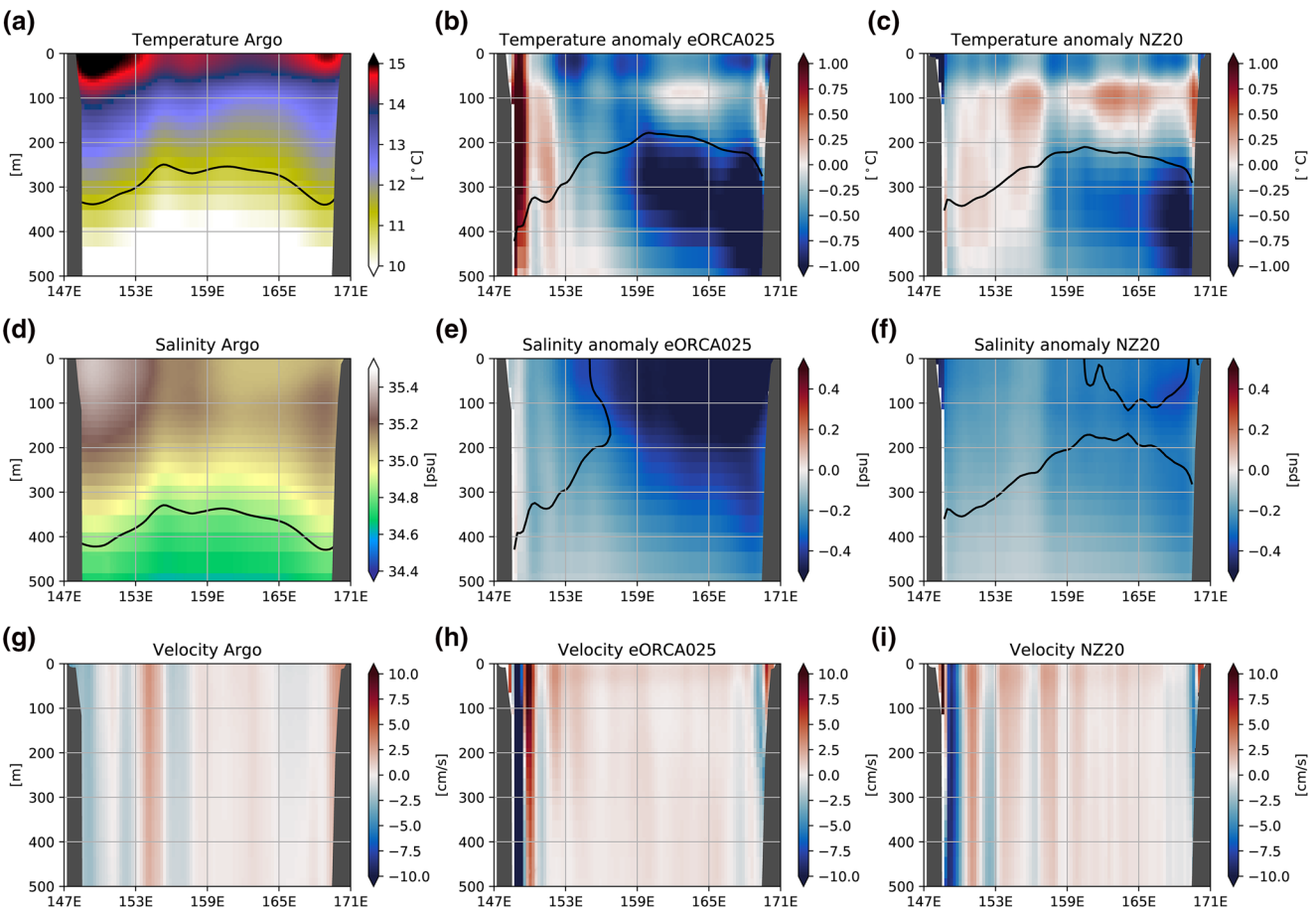
3.4.2. Tasman South Section

The Tasman South section runs in the zonal direction along 43°S across the Tasman Sea (Figure 6). The observed temperature (Figure 6a) shows elevated temperatures on both sides of the Tasman Sea, but warmer temperatures found near the Australian coast. Consequently, temperature in the center of the Tasman are cooler, which is also visible in the shallower 11°C isotherm. The warm water near Fiordland is part of the STF and the localized Fiordland Current along the New Zealand's west coast of the South Island (Behrens, Fernandez, et al., 2019; Chandler et al., 2019). In comparison, temperatures near the Australian coast are more than 1°C warmer in eORCA025 (Figure 6b) in line with positive temperature bias along the Tasman North section in this same depth range (Figure 5b). The remaining section is mainly characterized by a negative temperature bias of around −0.2°C in the top 200 m but exceeding −1°C below 200 m east of 159°E. The temperature bias in NZ20 (Figure 6c) are overall smaller compared to eORCA025. In particular, near the Australian coast where the temperature bias in NZ20 are close to zero. This is in contrast to eORCA025 which shows a large (>1°C) positive temperature bias in this region. Consequently, the 11°C isotherm in NZ20 model matches better with Argo.

The observed salinity structure shows similar features to temperature with highest salinity values found on either side of the Tasman Sea, but highest (>35.4 psu) near the Australian coast. The salinity bias in eORCA025 (Figure 6e) are negative over the entire section but, become larger closer to New Zealand and exceed −0.4 psu in the top 200 m. This negative bias is larger than along the Tasman North section (Figure 5e). While NZ20 also shows a negative salinity bias over the entire section (Figure 6f) the magnitude barely exceeds −0.15 psu.

The mean cross-section velocities in Argo are in the order of ±1–2 cm/s (Figure 6g). Southward (negative) velocities near Australia are visible, representing a part of the Tasman Sea Outflow fed by the EAC Extension. To the east, the current direction is alternating, but mainly positive east of 158°E, which is expected for the weak flow associated with the STF between 165° and 168°E in the top 200 m (Ridgway & Dunn, 2003; Stramma et al., 1995). The current structure from both models agrees with the general observed pattern, except near the coast where modeled velocities are higher. In particular, in eORCA025, velocities as part of the EAC Extension are stronger and the southward (negative) flow more concentrated along the Australian coast compared to Argo and NZ20. The outflow associated with the STF is visible in both models near the coast of Fiordland with flow speeds of around −5 cm/s.

The difference between net volume transports across Tasman North and South section varies between 1.5% and 3% due evaporation and transport through Bass and Cook Strait (Table 2). For heat transport, it varies between 38% and 43% for eORCA025 and NZ20, respectively. Despite the lower net heat transports in NZ20, its imbalance is larger and leads to a reduction of the cold bias compared to eORCA025 over the Tasman Sea.

Figure 6. Time mean (2004-2018) observed (a) temperature, (d) salinity, (g) cross section velocity along the Tasman South section from Argo. The cross-section velocities in Argo are based on the geostrophic flow with level of no motion at 2000m. Biases in temperature and salinity to Argo for (b, e) eORCA025 and (c, f) NZ20, respectively. Modelled cross-section velocities for (h) eORCA025 and (i) NZ20 are shown in comparison to Argo. Northward velocities have a positive sign. The Tasman South section starts at the Australian coast (148°E) and ends at the coast of Fiordland on the west of the South Island of New Zealand. Black contour lines show the 11°C and 34.8 psu contour, respectively.

3.4.3. 165°E Section

This meridional section is used as an example to illustrate the location of the STF_{TEMP} and STF_{SALT} in the Tasman Sea from Argo and both models (Figure 7). This location also allows us to measure the impact of the model bias, since the salinity bias in this region is large (Figure 4). The time-mean 11°C isotherms of Argo, eORCA025 and NZ20 are shown in Figure 7a, with the ±1°C range shaded. Over the upper 200 m, there is a good agreement between all data sets. The location of the STF_{TEMP} based on the 11°C isotherm (hexagons) in NZ20 and Argo are nearly a perfect match, while the STF_{TEMP} in eORCA025 is shifted slightly north, since eORCA025 is slightly colder.

The salinity discrepancy between Argo and the models is larger. As seen in the salinity biases (Figures 4a and 4b), both models show a fresh bias in the subtropical waters over the upper 200 m of the Tasman Sea. The same behavior is seen along this meridional section and the 34.8 psu isohaline is shifted around 4°–5° to the north in both models. Conversely, the vertical structure, and particularly the presence of a subsurface maxima, is consistent between Argo and both models. Argo and NZ20 show this subsurface maximum between 100 and 150 m depth, while it is found around 220 m depth in eORCA025. This difference causes the STF_{SALT} to be slightly further north in eORCA025 compared with NZ20.

The model evaluation has demonstrated that NZ20 performs better in several STF-related diagnostics than eORCA025 (e.g., reduced model biases in the STF region). The main shortfall of eORCA025 is the overly
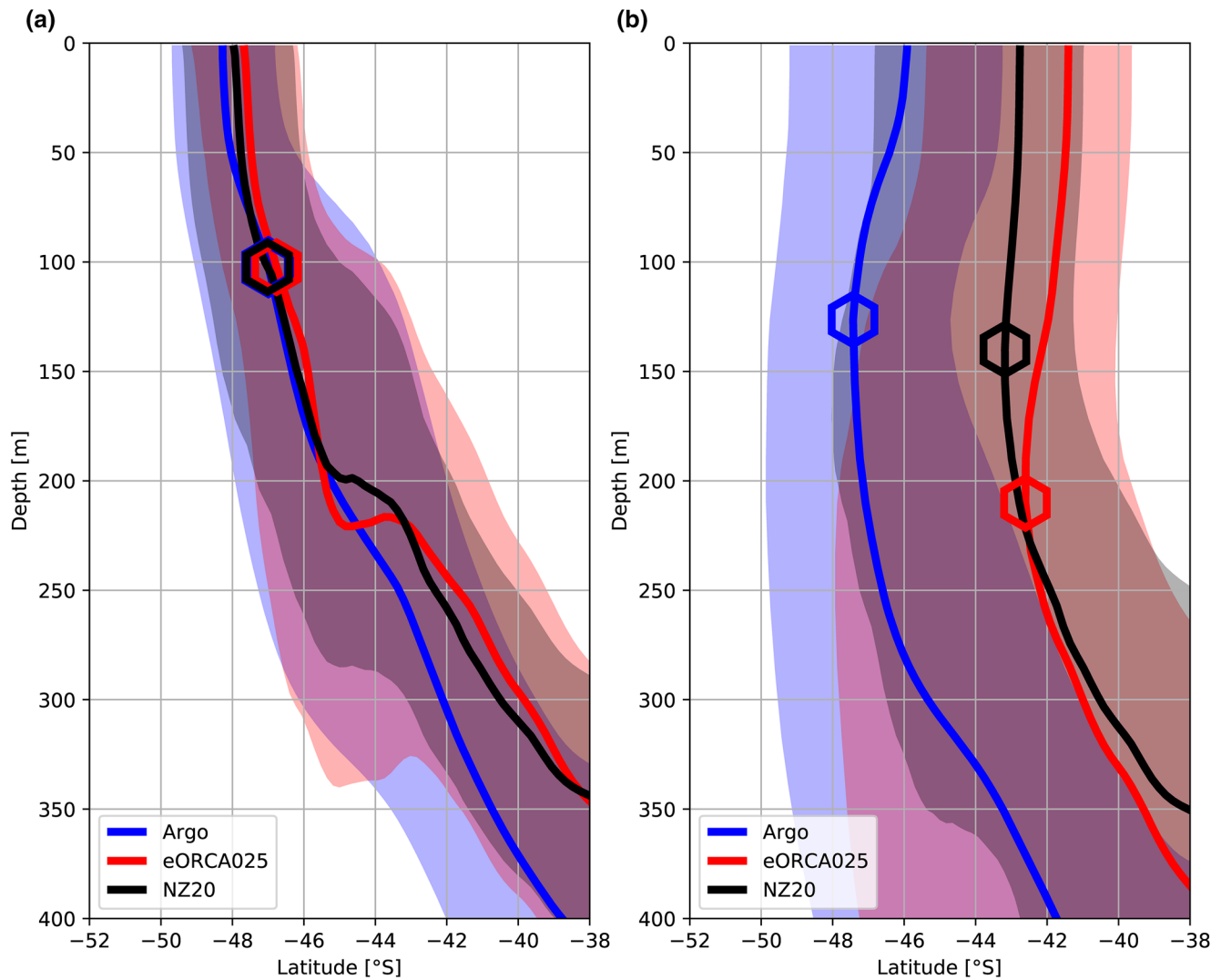
Figure 7. Meridional section along 165°E through the Tasman Sea. (a) Time mean (2004-2018) 11°C isotherm shown by the solid lines and ±1°C deviation by the color shading. (b) Time mean (2004-2018) 34.8 psu isohaline shown by the solid lines and ±0.2 psu deviation by the color shading. The hexagons show the location of the STF according to the isotherms and isohalines.

stable EAC Extension, which contributes to temperature and salinity biases over the Tasman Sea and impacts the location of the STF in the model. In the remainder of this study, we will therefore only present NZ20 results, which arguably performs better in simulating the STF.

4. Characterization of the STF in Space and Time

In the following section we present the mean modeled STF location over our target region and compare it against observations. In addition, we also investigate the meridional variability from seasonal to interannual timescales of the STF and propose potential drivers of STF variability on interannual time scales.

4.1. Mean Location of the STF

The mean location for the STF$_{TEMP}$ and STF$_{SALT}$ from Argo and NZ20 is shown over our target region in Figure 8. Since we use fixed temperature and salinity values over the entire domain, the STF detection around New Zealand comes with some caveats. Horizontal and vertical mixing within the boundary currents and freshwater input from rivers change the temperature and salinity structure along the coast. This issue
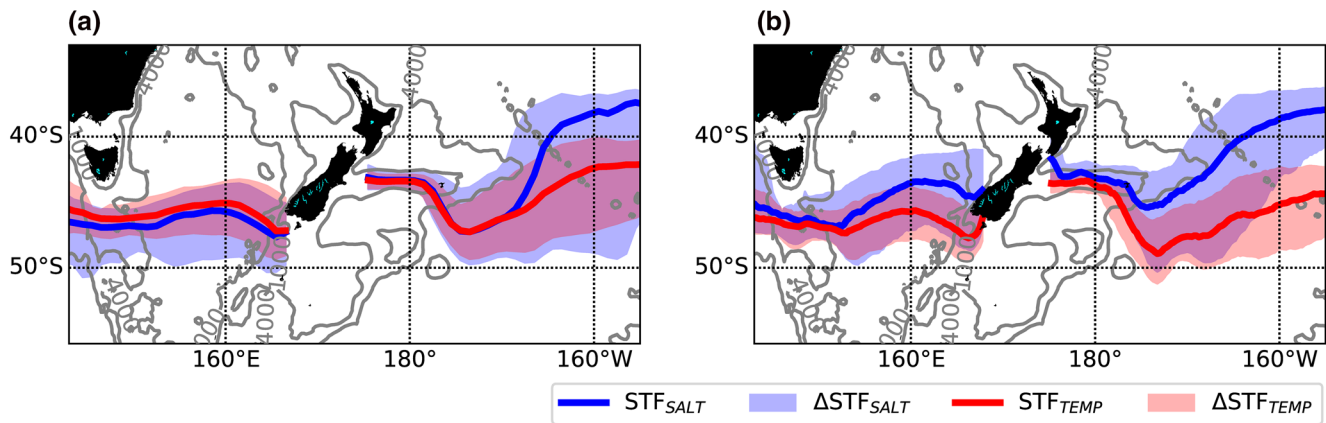
Figure 8. Time mean STF locations for Argo (a) and NZ20 (b) shown as solid lines for the period from 2004 to 2018. Colour shading in (a and b) shows the range in STF location with small deviations in the STF temperature (±1 °C) and salinity (±0.2 psu) thresholds.

becomes more relevant in NZ20, when the boundary currents are better resolved than currently available from Argo due to the dynamic nature of those currents and the low Argo density in them. Consequently, the detection algorithm indicates that the STF passes through Cook Strait, which is an unrealistic consequence of our STF detection technique. Therefore, we discard the STF locations within 60 km of the New Zealand coast.

The STF_{TEMP} (red line and shading in Figures 8a and 8b) runs south of Tasmania across the Tasman Sea and south of New Zealand with little change in its latitudinal position. To the east of New Zealand, the STF_{TEMP} follows the Chatham Rise, then veers southeast by ∼3°–4° in latitude, before veering northwards again. There is a good agreement between Argo and NZ20 for the location of the 11°C isotherm and the ±1°C range over the Tasman Sea and Chatham Rise. East of the rise the modeled STF_{TEMP} is shifted around 2° in latitude south compared to Argo, while the overall ±1° temperature envelope is similar to Argo.

In Argo the STF_{SALT} is located slightly south (∼1° in latitude) compared to the STF_{TEMP} over the Tasman Sea (Figure 8a). Whilst over the Chatham Rise the STF_{SALT} and STF_{TEMP} are very close to each other until 170°W. Further to the east the salinity and temperature estimates of the STF diverge from each other and STF_{SALT} shifts northward, reaching latitudes of about 38°S at 160°W. The salinity envelope (blue shading) highlights several regions where the STF_{SALT} position is sensitive to the choice of the reference salinity. Over the Tasman Sea, the envelope is around 5° in latitude wide. To the east of the New Zealand the envelope is initially very narrow (2° in latitude), but exceeds 15° in latitude east of the Chatham Rise at around 160°W. Large variability has been documented in this region where the STF approaches the SAF (Fernandez et al., 2014). This large range at 160°W is caused by a split in the flow of subtropical waters downstream from the Chatham Rise, and the subsurface maxima in salinity. A southern branch continues slightly north of 50°S, while a northern branch follows the 4000 m depth contour north, until this contour turns northwest around 170°W (not shown). The envelope is larger to the south of the mean STF_{SALT} location (34.8 psu), which reflects a weaker salinity gradient within the subantarctic water than in the subtropical water. The mean STF_{SALT} location in NZ20 shows a northward displacement compared to Argo (Figure 8b). Over the western Tasman the difference is around 2° in latitude but increases up to 4° in latitude when approaching Fiordland. Over the Chatham Rise the difference is small, but the modeled STF_{SALT} does not shift as far south as the Argo defined STF_{SALT} does east of the rise. The modeled ±0.2 psu salinity envelope range is similar to Argo when taking the general northward displacement into account. In eORCA025 this mismatch to Argo is larger, due to the larger model salinity and temperature biases in these regions (therefore it is not shown).

### 4.2. Seasonal Variability of the STF

In the following section, we investigate the seasonal meridional variability using Hovmöller plots (Figure 9). The seasonal variability for STF_{TEMP} is very coherent between Argo and NZ20 (Figures 9a and 9b).
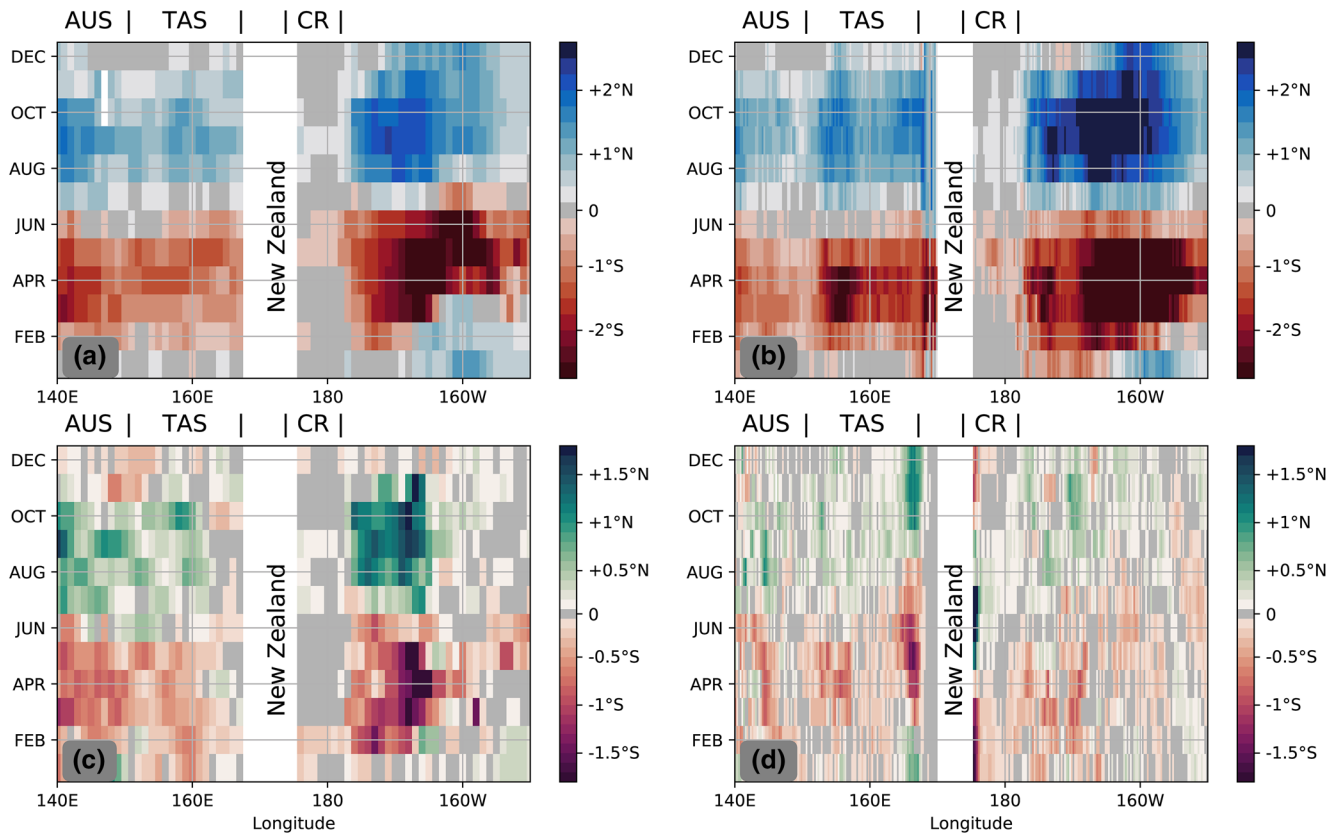
Figure 9. Seasonal meridional variation of the STF for Argo data (left panels) and NZ20 (right panels) over the period 2004 to 2018. STF$_{TEMP}$ (a, b) and STF$_{SALT}$ (c, d). The zonal range of Australia (AUS), Tasman Sea (TAS) and Chatham Rise (CR) are shown by the respective labels on the top.

Both, Argo and NZ20 show a more northward location (blue shading in Figures 9a and 9b) of STF$_{TEMP}$ during austral winter and spring months (July–November) reaching its most northern limit in September to October. A southward shift (red shading in Figures 9a and 9b) of the STF$_{TEMP}$ occurs during austral summer and autumn months (February–June). The southernmost location is reached between March and May. The meridional range is larger east of the Chatham Rise compared to the range in the Tasman Sea, which agrees with the larger ±1°C envelope east of the Chatham Rise (Figure 8). In Argo the range is around 3° in latitude in the Tasman Sea, while it is up to 6° in latitude east of the Chatham Rise. The range in NZ20 in both regions is higher, up to 4° and 8° in latitude in the Tasman Sea and east of the Chatham Rise, respectively. Some of this larger range may be related to the finer horizontal resolution of NZ20 compared to Argo.

The seasonality of the STF$_{SALT}$ in Argo (Figure 9c) follows the STF$_{TEMP}$ behavior, with a more southward location (red shading) during austral summer and autumn and a northward shift (green shading) during austral winter and spring in most regions. The seasonal range in the Tasman Sea is around 2° in latitude, with a southward maximum during late austral summer (February–April). Over the Chatham Rise, the range is reduced to 0.5° in latitude. East of Chatham Rise, in the South Pacific, the seasonal range increases to 3°–4° in latitude until 160°W. The seasonal signal in NZ20 appears to be impacted by the misplaced STF$_{SALT}$ over most of the region. As a result of the this misplaced STF$_{SALT}$, the seasonal range in NZ20 is significantly reduced to less than 1° in latitude, although the general seasonal pattern, a northward and southward shift during the seasons, is captured. An elevated seasonal signal is present near Fiordland, along the West Coast of New Zealand. Here the misplaced STF$_{SALT}$ in NZ20 captures the seasonality of the river discharge from the Southern Alps into the Tasman Sea. During April–July, the river flow is lowest due to the snow accumulation on the Southern Alps (Kerr, 2013) causing the southward shift of the STF$_{SALT}$, while late spring is characterized by elevated snow melt and consequently a northward shift of the STF$_{SALT}$. NZ20 does not capture the elevated seasonal range east of the Chatham Rise, since the STF$_{SALT}$ does not dip south into the confluence zone of STF and SAF as seen in the Argo data.
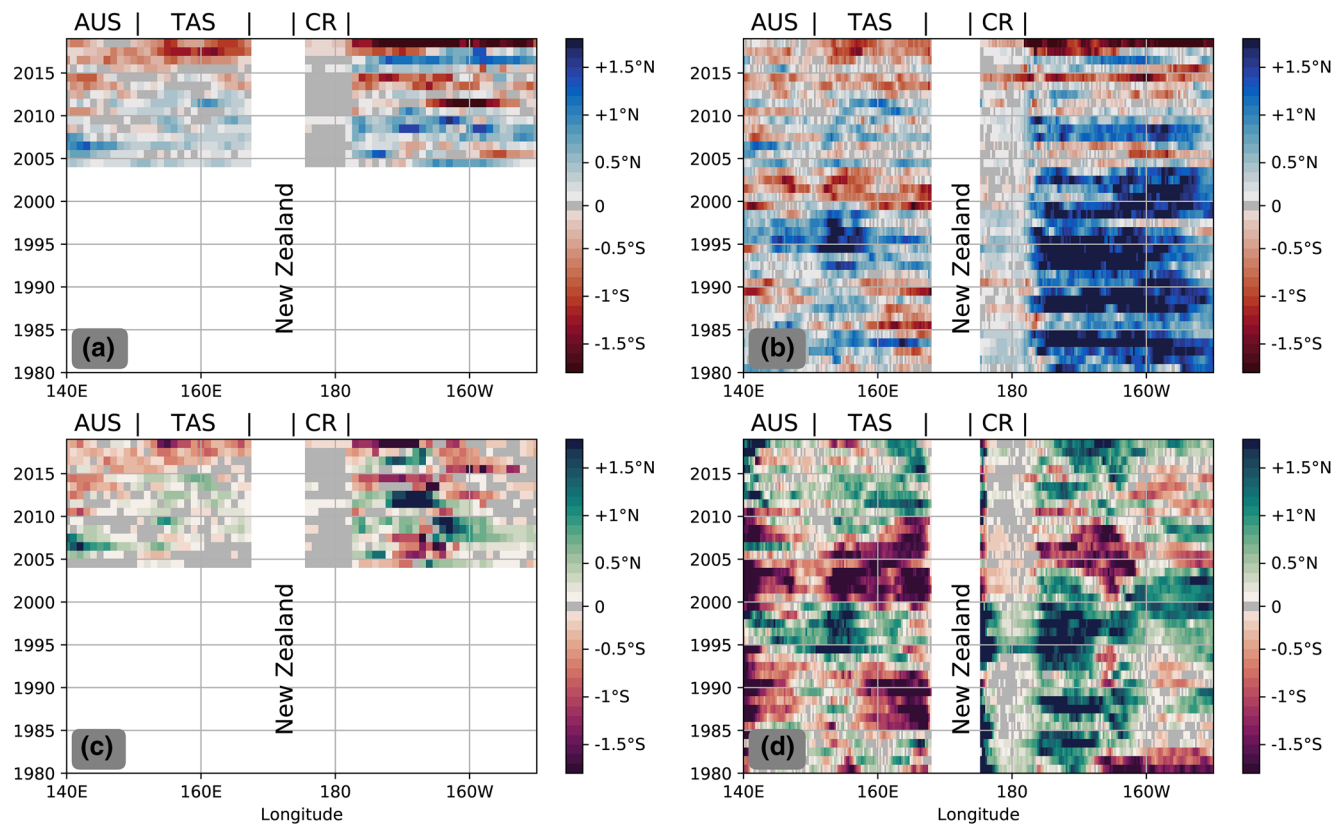
Figure 10. Interannual meridional variation of the STF for Argo (left panels) and NZ20 (right panels). Over the period 1980 (2004, Argo) to 2018. STF_{TEMP} (a, b) and STF_{SALT} (c, d). The zonal range of Australia (AUS), Tasman Sea (TAS) and Chatham Rise (CR) are shown by the respective labels on the top.

4.3. Interannual Variability of the STF

On interannual time scales, based on deseasonalized annual means, we observe meridional shifts of the STF_{TEMP} and STF_{SALT} of about 2° in latitude from its mean location in Argo (Figures 10a and 10c). Over the Tasman Sea, the Argo shows an overall southward shift of the STF_{TEMP} of about 1°–2° in latitude since 2004, although this is not zonally uniform. A similar tendency is present in STF_{SALT} in this region, which suggests saltier and warmer subtropical waters flowing into this region, perhaps as a result of an southward expansion of the Super-Gyre (Hu et al., 2015; Sen Gupta et al., 2016; Yang et al., 2020). East of the Chatham Rise the interannual variability is higher which limits the detection of trends in STF_{TEMP} and STF_{SALT} over the Argo period. Interannual variability west and east of New Zealand does not appear to covary.

In comparison to the Argo, NZ20 shows a similar southward tendency for STF_{TEMP} in the Tasman Sea, but no clear southward trend is present for STF_{SALT} (Figures 10b and 10d) over this period from 2004 to 2018. In addition, NZ20 simulates similar interannual signals for STF_{TEMP} to Argo in the Tasman Sea and east of the Chatham Rise, while only limited co-variability between signals east and west of New Zealand exists. Furthermore, the longer STF timeseries from NZ20 suggests considerable variability on timescales of 5–10 years west and east of New Zealand, which cannot be captured by the shorter Argo record. For example, NZ20 simulates a northward shift of STF_{TEMP} and STF_{SALT} from 1994 to 2000 of about 1° in latitude over most of the Tasman Sea with a reversed southward shift from 2000 to 2004 of about −0.75 to −1° in latitude in STF_{TEMP} and STF_{SALT}. We note that the modeled STF_{SALT} results need to be treated with caution due to the large fresh bias in the model and misplaced STF_{SALT}. Observations along the SR3 hydrographic section, south of Tasmania, also documented a northward shift of the STF during 1996 (Sokolov & Rintoul, 2002), which aligns with the model results. Large interannual signals are also present east of the Chatham Rise in NZ20 in the order of 3° in latitude. In addition to this interannual variability in NZ20 the STF_{TEMP} shows a southward shift east of the Chatham Rise of around 3° in latitude between 1980 and 2018, which is not apparent when only the 2004–2018 period is considered. Some of this trend could be linked to observed

warming trend in this region which has been attributed to a large scale dynamic gyre response (Roemmich et al., 2007, 2015, 2016). The long-term trend of STF_{TEMP} in the Tasman Sea in NZ20 is weaker than the trend east of the Chatham Rise over the hindcast period from 1980 to 2018. We note that the modeled STF_{SALT} does not show any trend over this period in both regions. However, we recognize some co-variability between STF_{SALT} and STF_{TEMP} in the Tasman Sea in NZ20. Here a southward shift between 1986–1991 and 2000–2005, accompanied with northward shifts before, during and after, are present in STF_{SALT} and STF_{TEMP} and suggest links to the large-scale gyre variability. Therefore, we test how basin-wide changes in the subtropical gyre circulation, meridional transport and the extent of subtropical water can be linked to the location of the STF in the Tasman Sea in the following section.

4.4. Upper 500 m Heat and FW Content Changes in the Tasman Sea

In the following section, we investigate the drivers of the meridional shifts of the STF, linking them to dynamical changes in the transport of heat and freshwater into the Tasman Sea (the enclosed region of Tasman North and South sections). We focus on the NZ20 model results for transport calculations, as we cannot obtain robust transport estimates from the Argo data. More sophisticated observational datasets and analysis are required to capture dynamic boundary currents and their transport (Sloyan et al., 2016; Zilberman et al., 2018) which is beyond the scope of this study. Figure 11a shows the freshwater transport anomalies across both control sections, Tasman North (orange) and South (blue). The timeseries show large interannual variability, of about ±0.02 Sv for Tasman North. With only a few exceptions, Tasman North anomalies are larger than Tasman South transport anomalies. The period from 1986 to 1991 is significant, because freshwater transport anomalies of the Tasman North section are large and persistently southward. The opposite is true for the period 1996–1999. A second period with strong southward freshwater anomalies in the Tasman North transports is the period 2005–2011. Some of these periods align with periods when the STF_{SALT} showed large persistent anomalies in the Tasman Sea (Figure 10d).

We calculate the NZ20 freshwater transport contribution to 0–500 m freshwater content over the Tasman Sea (enclosed region of Tasman North and South), assuming a constant surface flux. We compare this freshwater content estimate (color shading) against the true modeled (solid teal line) 0–500 m freshwater content anomalies in Figure 11b. The freshwater transport anomalies to the freshwater content can reproduce most of the interannual to decadal signals of the modeled freshwater content anomalies, which indicates that interannual variability of surface fluxes are of minor importance for the overall budget. Between 1986 and 1995 the freshwater content anomaly becomes progressively more positive and reaches a maximum in 1995 of about 1.2×10^{12} m³, before turning negative with a minimum of around -2×10^{12} m³ in 1999 (note the reversed y-axis). Over the period from 2005 to 2011 the modeled freshwater content increases constantly until 2011, reaching similar values as in 1995. Over the last few years (2015–2017) the modeled freshwater content was nearly neutral with a positive anomaly in 2018. The Argo freshwater content anomaly (black line) shows similar decadal signals, but with a lower freshwater content over the past few years (2015–2018). So, despite the large fresh bias in NZ20 and northward shifted STF_{SALT}, interannual to decadal freshwater content anomalies align with Argo. Freshwater content anomalies are connected with the STF_{SALT} over the Tasman Sea sector for Argo and NZ20, as indicated by color-coded dots on top of the freshwater content timeseries. During periods when the freshwater content anomaly is positive the STF_{SALT} is found further north compared to during negative phases. Exceptions occur during 1981–1983, 1999–2001 and 2016–2017 when the freshwater content shows the opposite sign to the STF_{SALT} anomalies.

Similar to the freshwater transports, the Tasman North heat transports are larger than the Tasman South, which highlights their importance as a driver for variability, and indicates that the Tasman Sea loses heat to the atmosphere (Figure 11c). The period from 1990 to 1996 can be identified as period with persistent northward heat transport anomalies across Tasman North and Tasman South, with the opposite phase from 1997 to 2000, and 2012 to 2016. Some of these periods overlap with persistent periods of freshwater transport anomalies, suggesting a coupling on long time scales. The remaining timeseries shows larger year to year variability, compared with the freshwater transports.

The NZ20 heat transport contribution to the 0–500 m heat content anomalies (color shading Figure 11d), captures the true modeled heat content anomalies (orange curve) in large parts. The Argo timeseries (black curve) is very similar to the modeled heat content changes. We can identify a persistent cold period from
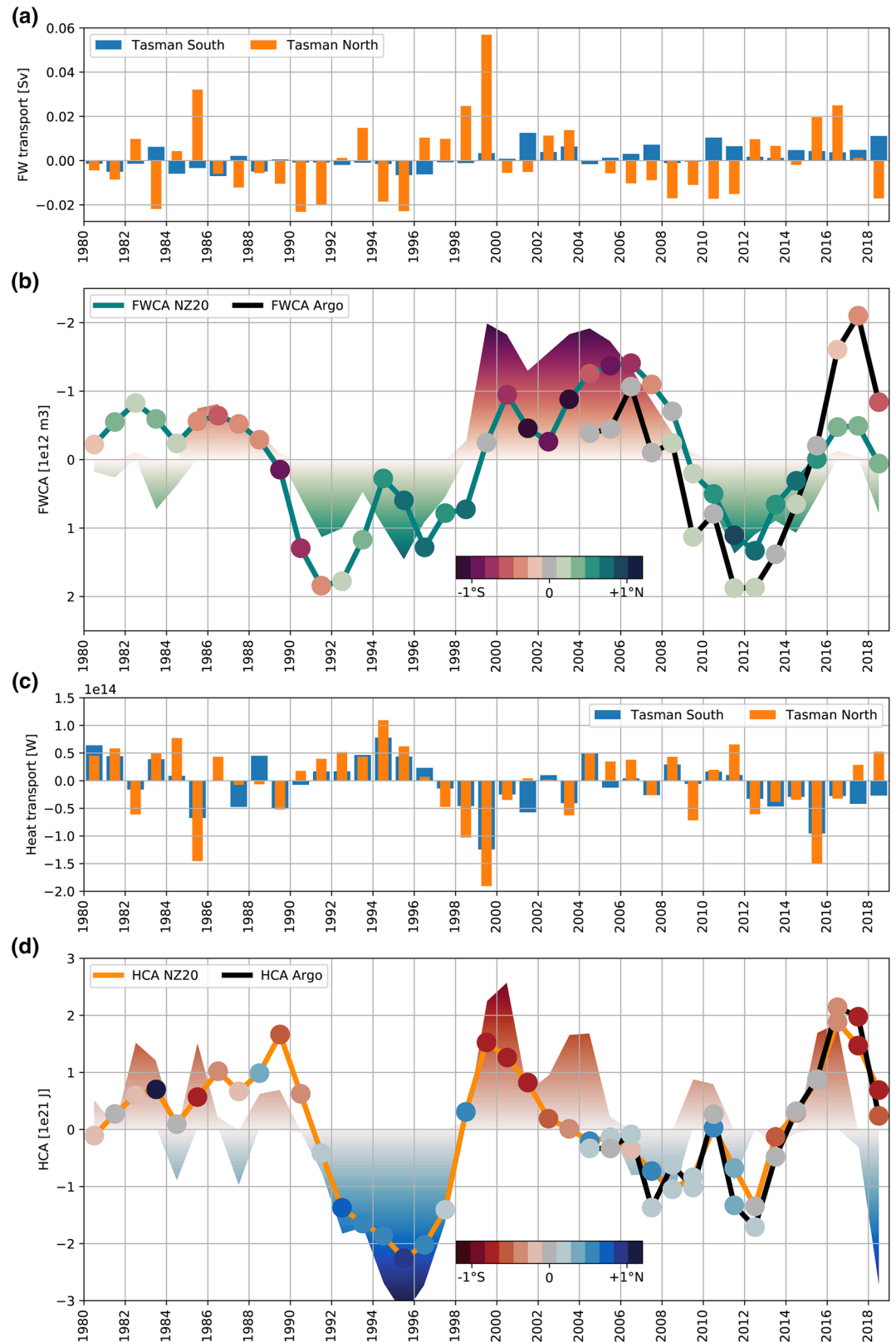
Figure 11. Annual mean time series of integrated 0 – 500m (a) freshwater transport across TN and TS, (b) freshwater transport contribution to the freshwater content anomaly (color shading), true freshwater content anomaly (FWCA, Sref=34.8) from NZ20 (teal) and Argo (black). The color-coded dots show the meridional anomaly of the STF locations over the Tasman Sea. (c) and (d) the same diagnostic but for heat transport and heat content anomaly (HCA).

1990–1998, which aligns with the predominantly northward heat transport anomalies across Tasman North and Tasman South and causing the heat content to drop. Some of this cold period can be linked to the eruption of Pinatubo in 1991, which led to a widespread cooling signal (Basher & Thompson, 1996; Hansen et al., 1996; Parker et al., 1996; Sutton & Chiswell 1996). The heat content anomaly minimum is reached in 1995 with -3×10^{21} J, but rebounds rapidly to a positive heat content anomaly with a maximum of around 2×10^{21} J in 2000. Similar interannual signals have been documented as part of a heat content budget between Sydney, Wellington, Auckland and Suva using XBT profiles (Roemmich et al., 2005). These observations show a minimum in upper ocean heat content in 1995 and a maximum in 2001 (Figure 8b in Roemmich et al., 2005 and Figure 3 in Sutton et al., 2005). Since 2000 the heat content shows a negative trend until 2012, when it reversed and exhibits elevated positive anomalies for the period 2015 and 2016. Some of this negative heat content trend from 2000 to 2012 might be linked to a negative Interdecadal Pacific Oscillation and a reversal to a positive phase since 2011 (Dong & Dai, 2015; Meehl et al., 2016; Salinger et al., 2001). We note that freshwater content anomaly also showed a reversal during that period. For 2017 and 2018 the heat transport contribution to the heat content has declined to similar values as seen in 1995, with the true modeled heat content (solid lines) also following this trend. The location of the STF_{TEMP} over the Tasman Sea (color-coded dots over the heat content timeseries) follows the heat content anomalies and the STF_{TEMP} is found further south during periods when the heat content anomaly is positive and further north when the heat content anomaly is negative.

Attempts to robustly link freshwater and heat content anomalies over the Tasman, and the location of the STF, to large-scale climate drivers, such as El Niño Southern Oscillation (ENSO) and the Interdecadal Pacific Oscillation have not been successful (not shown). We found some similarities between the individual timeseries for certain periods, like the decline (increase) in the heat (freshwater) content and the Interdecadal Pacific Oscillation as described above but not robustly over the entire model hindcast period. We acknowledge that none of these climate drivers is acting alone, which makes the attribution of specific events to individual climate oscillations challenging.

The NZ20 model simulations demonstrate that heat and freshwater transports over the top 500 m across the Tasman North section covary, and dominate the interannual variability in this region, in alignment with previous results (Behrens & Fernandez et al., 2019). Therefore, the top 500 m heat and freshwater content over the region shows similar long-term variability, and consequently the position of STF_{TEMP} and STF_{SALT}. This result is consistent with the hypothesis that warm and saline anomalies are advected into the Tasman Sea across the northern boundary and affecting the heat and freshwater content over this region and beyond and may result in a southward shift of the STF over this region. Conversely, cool and fresh anomalies result in a northward shift.

4.5. Local and Regional Wind-Stress Curl as Driver for Variability

Lead-Lag correlations between the upper 500 m heat transport contribution to the heat content, SST, absolute dynamic topography, and wind stress curl have been performed (Figure 12). We only consider positive correlations and lead times for SST, absolute dynamic topography, and wind stress curl, so they are in phase with the heat content anomalies. Results for the correlation maximum between SST and heat content anomalies (Figure 12a) show the highest correlation ($r > 0.6$) near Tasmania, and correlations between $r = 0.4$ and $r = 0.5$ over most parts of the Tasman Sea (orange box). Correlations of around $r = 0.5$ are also visible to the north east of North Island of New Zealand. The lead times for these correlations do barely exceed 0.5 years over the Tasman Sea. Lead times to the north east of New Zealand vary between 1 and 3 years. For absolute dynamic topography (Figure 12b) most of the Tasman Sea is characterized with correlations higher than $r = 0.6$ and highest corrections are found in the center of the Tasman Sea. Elevated ($r > 0.4$) correlations are also present to the north east and east of New Zealand. The lead times of these correlations (Figure 12e) in the Tasman Sea decrease from one year near New Zealand to zero near the Australian coast and suggesting westward Rossby wave propagation (Bowen et al., 2006). A portion of this propagation can be traced further to the east of New Zealand with lead times up to three years. That suggest that some signals originate from the Tasman Sea, while others propagate into the Tasman Sea as Rossby waves. Remotely forced impacts on the Tasman Sea, EAC and EAC Extension have been already identified by previous studies (Hill et al., 2010; Holbrook et al., 2011; Li et al., 2020). Significant correlations between wind stress curl
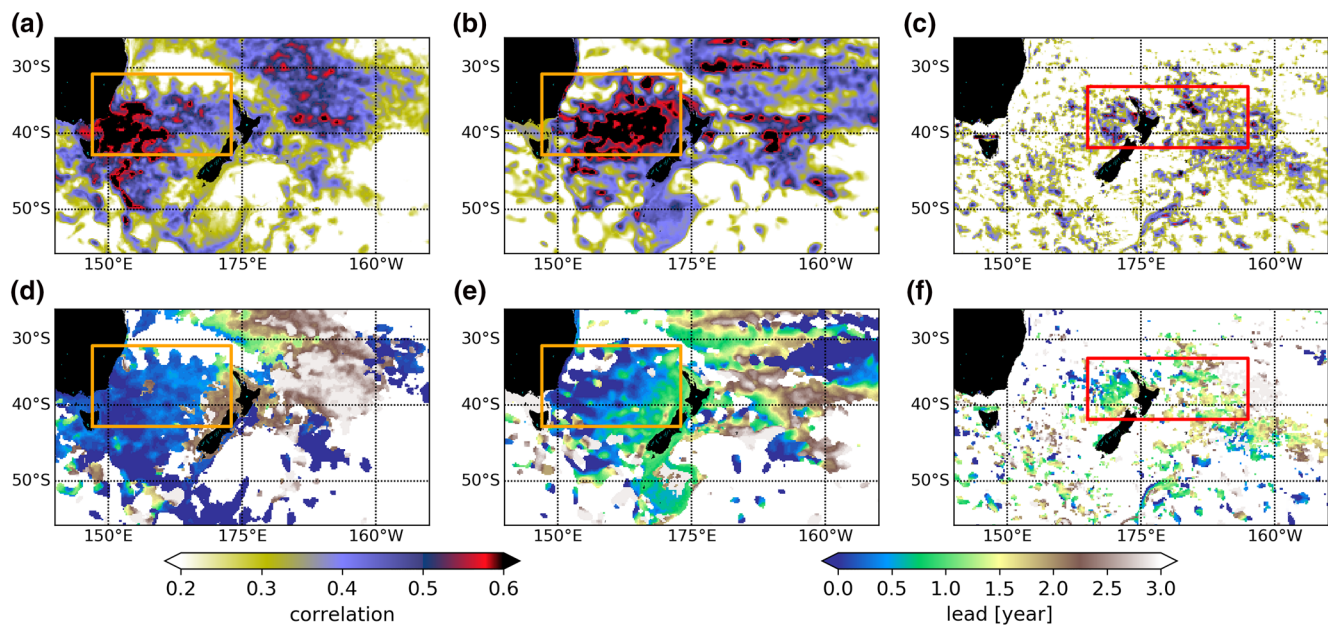
Figure 12. The correlation maximum between integrated 0–500m Tasman Sea heat transport contribution to the heat content and (a) SST, (b) absolute dynamic topography and (c) wind stress curl over the period from 1980 to 2018. (d-f) Is showing the lead times of these maximum correlations in years for (d) SST, (e) absolute dynamic topography and (f) wind stress curl. The orange (red) box marks the region for area averages for SST and absolute dynamic topography (wind stress curl) for Figure 13. Only significant correlations ($p \leq 0.01$) and lead times are shown.

and heat content anomaly (Figure 12c) are less coherent than for SST and absolute dynamic topography. However, regions with elevated correlations of about $r = 0.4$ can be identified in the eastern Tasman Sea and east of the North Island, to as far as 165°W. Lead times of wind stress curl (Figure 12f) roughly match lead times of absolute dynamic topography, of around one year in the eastern Tasman Sea and up to 1.5 years to east of New Zealand.

The area-averaged timeseries of SST, absolute dynamic topography and wind stress curl over the highlighted regions in Figure 12 are shown in Figure 13. Modeled SST (orange line, $r = 0.58$) and absolute dynamic topography (teal line, $r = 0.74$) anomalies follow the heat content anomaly based on oceanic transports over the upper 500 m (color shading). Observed absolute dynamic topography (black line) shows similar long-term variability to the model results. The link between wind stress curl (purple bars, $r = 0.49$) and heat content changes is weaker, but strong and/or persistent heat content changes can be associated with them, like the transition from negative to positive heat content anomalies around 1998, where persistent negative wind stress curl anomalies are present until 1998 but turn strongly positive afterward. Changes in the wind stress curl impact Ekman transports and trigger westward propagating Rossby waves (Bowen et al., 2006). In general, negative wind stress curl anomalies are associated with Ekman divergence, negative heat content anomalies and a drop in absolute dynamic topography and SST. The low correlations indicate that these wind stress curl changes are not the solely driver for heat content anomalies over the Tasman Sea. Rossby waves also impact the heat content by changes in the depth of the isotherms and when influencing the transport of the western boundary currents (Hill et al., 2010; Holbrook et al., 2011; Li et al., 2020).

5. Discussion and Conclusion

We have demonstrated that the high-resolution (1/20°) two-way nested model (NZ20) has reduced model biases of temperature and salinity (Figure 4) and captures the oceanic circulation around New Zealand better than a global ¼° model (eORCA025). Consequently, the NZ20 modeled location of the STF and temporal variability of the STF aligns better with observations from AVISO and Argo than with eORCA025. However, a large fresh bias in NZ20 around New Zealand still remains. This bias leads to a northward displacement of the STF in the modeled STF_{SALT}, compared with the observed STF_{SALT}. A better agreement between modeled
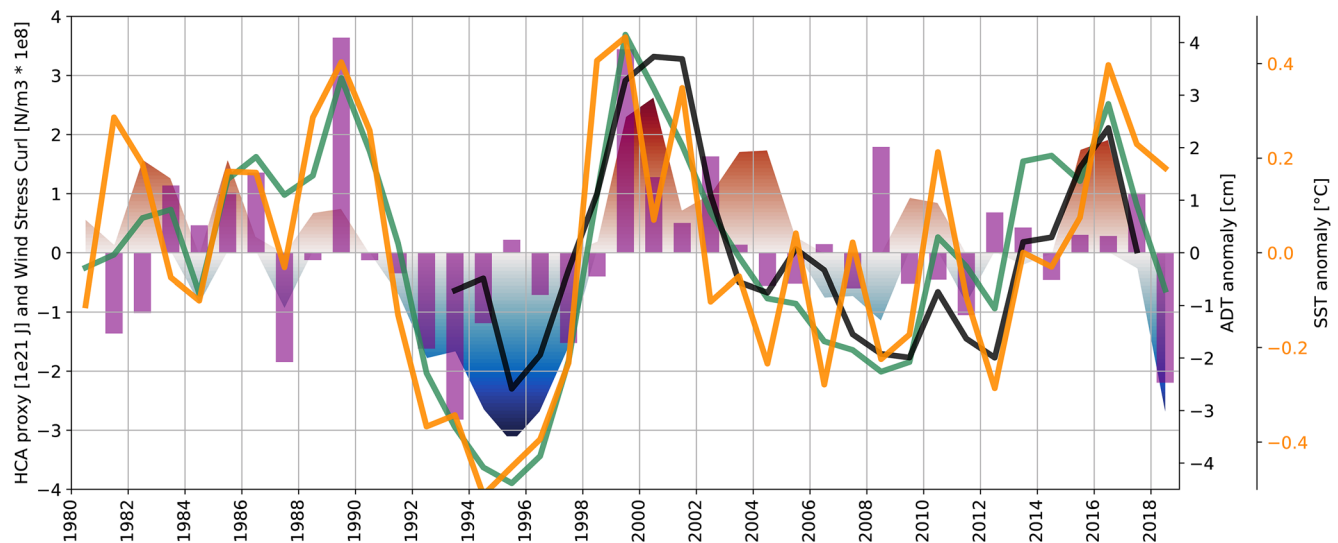
Figure 13. Estimated 0–500m Tasman Sea heat content anomaly, based on heat transport anomalies, represented by the color shading. Area averaged modelled (green line) and observed (black line) absolute dynamic topography (first right y-axis), SST (orange, second right y-axis) and winds stress curl (purple bars, left y axis). Regions over which the quantities have been averaged are shown in Figure 12. Note, one-year lead time has been applied to the wind stress curl anomalies and linear trends have been removed from all timeseries.

and observed STF on both seasonal and interannual scales when the STF location is based on temperature (Figure 10). For example, the reported northward shift of the STF_TEMP along the SR3 hydrographic section south of Tasmania in 1996 (Sokolov & Rintoul, 2002) is well represented in NZ20. The better performance of NZ20 over eORCA025 suggests that increasing the resolution in order to better simulate the boundary current dynamics and mesoscale eddies is important to capture the temporal variability in this region. Other modeling studies have come to similar conclusions, with improved performance of models with higher model resolution (Bull et al., 2017; Kiss et al., 2020; Oliver et al., 2015).

The data from Argo and the NZ20 model show that the STF around New Zealand varies not only on seasonal time scales, but also on interannual to decadal time scales. However, the seasonal cycle dominates the meridional shift of the STF, which can reach up to 6° (650 km) in the open ocean as a result of seasonal atmospheric heating. In terms of seasonal STF variability, our results are consistent with previous studies, which suggest seasonal shifts between 1° and 4° in the Southern Ocean (Graham et al., 2012; Kim & Orsi, 2014; Sallée et al., 2008; Sokolov & Rintoul, 2009b). These shifts in the STF are significantly reduced (0.5°–1° in latitude) in regions where the STF encounters bathymetry, such as the Chatham Rise (Figures 9 and 10). Along the Chatham Rise we observe large transports of adjacent subtropical and subantarctic water masses, which cause large persistent gradients in water mass properties. This appears to increase the effect of bathymetry on currents along the Chatham Rise to lock the STF to this feature (Sutton 2001). To the east of Chatham Rise the bathymetry drops and the flow forms eddies and meanders, which increase the variability of the STF and potentially make the STF more susceptible to external climate forcing and trends (Figure 8). This finding is consistent with previous studies showing larger variability of fronts in the open ocean compared with fronts closer to steep topography (Fernandez et al., 2014; Graham et al., 2012; Sallée et al., 2008; Sokolov & Rintoul, 2007, 2009b).

The Argo data show a southward trend of the STF position since 2004 in the Tasman Sea. NZ20 captures this trend in the Tasman Sea when the STF is based on temperature and suggest a southward shift of around 3° in latitude east of the Chatham Rise over the hindcast period from 1980 to 2018. However, the long hindcast of NZ20 also exhibits large meridional shifts of the STF in the Tasman Sea and east of the Chatham Rise on interannual to decadal time scales and raises the question of how much of the observed southward STF trend in Argo from 2004 onward, is part of interannual to decadal variability. The model results indicate that these southward shifts in the position of the STF in the Tasman Sea are influenced by heat and freshwater content anomalies in the Tasman Sea. Modulations in the upper ocean heat and freshwater content in the

Tasman Sea impact on the location of the 11° isotherm and the 34.8 psu isohaline in this region, which have been used to define the STF, following earlier studies (Orsi et al., 1995). However, the heat and freshwater content over the Tasman Sea, and the location of the STF are only indirectly coupled, due to the spatial distance between both.

The modeling results suggest that the heat and freshwater content anomalies in the Tasman Sea are dominated by oceanic transport and are a consequence of wind stress curl anomalies in the eastern Tasman Sea and east of New Zealand's North Island. Wind stress curl anomalies drive Ekman convergence or divergence and trigger westward propagating Rossby waves. During phases of positive wind stress curl, the Ekman transport converges, causing heat content to increase and the STF to move southward. The opposite behavior has been found for periods with negative wind stress curl with increased freshwater content, due to Ekman divergences, shifting the STF northward. These wind stress curl anomalies cannot explain the entire heat content variability and more drivers are involved. Rossby waves modulate heat and freshwater content by changing the depth of isotherms and isohalines and impacting the transport of western boundary currents, such as the EAC and EAC-Extension (Hill et al., 2010; Holbrook et al., 2011; Li et al., 2020). Transport anomalies within the EAC and across the northern boundary of the Tasman Sea are therefore the major driver of the STF shifts, while the magnitude of transport variability across the southern boundary is much smaller. Since the STF variability over the Tasman Sea is forced by local and regional drivers, it is imperative that ocean models can capture the local and regional scales realistically. Attempts to robustly link STF variability in the Tasman Sea to individual large-scale climate driver such as ENSO, and the Interdecadal Pacific Oscillation, was not successful over the hindcast period. None of these climate oscillations are acting alone and responses are not necessarily instantaneous, which makes the attribution of STF variability to them challenging. EAC transport anomalies and sea level near Sydney have been linked to ENSO and associated westward propagating Rossby waves (Holbrook et al., 2011). Further south the ENSO impact appears to weaken, while basin wide wind stress curl over the South Pacific has been been connected to transport changes through the Tasman Sea, temperature and salinity anomalies at Maria Island and South Pacific Gyre Circulation (Hill et al., 2008, 2011; Ridgway, 2007; Ridgway et al., 2008; Roemmich et al., 2007, 2016). But, uncertainty still remains how ENSO is affecting the wind stress curl anomalies (Hill et al., 2011) and therefore how variability over the entire Tasman Sea is connected to ENSO (Behrens, Fernandez, et al., 2019). We note that transport changes of the South Pacific Gyre circulation or within the EAC system do not neccessarily effect heat and freshwater content changes over the entire Tasman Sea, since they influence inflow and outflow simultaneously. More work is required to determine the origin of the wind stress curl anomalies, which drive anomalous oceanic transports.

In conclusion we have shown that a high-resolution ocean model is able to capture observed STF variability in the Tasman Sea and around New Zealand when temperature is used to define the STF. The STF variability is largest on seasonal time scales and in regions away from shallow bathymetry. The interannual to decadal STF variability south of the Tasman Sea is linked to fluctuations of heat and freshwater content within the Tasman Sea as a consequence of local and regional wind stress curl anomalies via Ekman transport and Rossby waves.

Connecting the meridional shifts of the STF to changes in heat and freshwater over the Tasman Sea allows for a more robust understanding of the drivers of variability, such as wind stress curl, on longer time scales. Furthermore, this improved understanding may provide a new paleo proxy for STF changes, using paleo SST from the northern Tasman Sea (e.g., from corals or marine sediment cores) to estimate potential changes in the paleo-STF.

Data Availability Statement

The data used for this manuscript can be publicly accessed through following link https://doi.org/10.5281/zenodo.3755270.

References

Barnier, B., Madec, G., Penduff, T., Molines, J. M., Treguier, A. M., Le Sommer, J., et al. (2006). 'Impact of partial steps and momentum advection schemes in a global ocean circulation model at eddy-permitting resolution. *Ocean Dynamics*, *56*, 543–567.

Basher, R. E., & Thompson, C. S. (1996). Relationship of air temperatures in New Zealand to regional anomalies in sea-surface temperature and atmospheric circulation. *International Journal of Climatology*, *16*, 405–425.

Behrens, E., Fernandez, D., & Sutton, P. (2019). Meridional oceanic heat transport influences marine heatwaves in the Tasman Sea on interannual to decadal timescales. *Frontiers in Marine Science*, *6*, 228.

Behrens, E., Williams, J., Morgenstern, O., Sutton, P., Rickard, G., & Williams, M. J. M. (2020). Local grid refinement in New Zealand's earth system model: Tasman sea ocean circulation improvements and super-gyre circulation implications. *Journal of Advances in Modeling Earth Systems*, *12*, e2019MS001996.

Belkin, I. M., & Cornillon, P. (2003). SST fronts of the Pacific coastal and marginal seas. *Pacific Oceanography*, *1*, 90–113.

Belkin, I. M., & Gordon, A. L. (1996). Southern Ocean fronts from the Greenwich meridian to Tasmania. *Journal of Geophysical Research*, *101*, 3675–3696. https://doi.org/10.1029/95JC02750

Bowen, M. M., Sutton, P. J. H., & Dean, R. (2006). Wind-driven and steric fluctuations of sea surface height in the southwest Pacific. *Geophysical Research Letters*, *33*, L14617. https://doi.org/10.1029/2006GL026160

Bull, C. Y. S., Kiss, A. E., Jourdain, N. C., England, M. H., & van Sebille, E. (2017). Wind forced variability in eddy formation, eddy shedding, and the separation of the east Australian current. *Journal of Geophysical Research: Oceans*, *122*, 9980–9998. https://doi.org/10.1002/2017JC013311

Butler, E. C. V., Butt, J. A., Lindstrom, E. J., Tildesley, P. C., Pickmere, S., & Vincent, W. F. (1992). 'Oceanography of the subtropical convergence zone around southern New-Zealand. *New Zealand Journal of Marine and Freshwater Research*, *26*, 131–154.

Cai, W. (2006). Antarctic ozone depletion causes an intensification of the Southern Ocean super-gyre circulation. *Geophysical Research Letters*, *33*(3), L03712. https://doi.org/10.1029/2005GL024911

Chandler, M., Bowen, M., & Smith, R. O. (2019). The Fiordland current, southwest New Zealand: Mean, variability, and trends. *New Zealand Journal of Marine and Freshwater Research*, 1–21.

Chiswell, S. M., Bostock, H. C., Sutton, P. J. H., & Williams, M. J. M. (2015). Physical oceanography of the deep seas around New Zealand: a review. *New Zealand Journal of Marine and Freshwater Research*, *49*(2), 286–317. https://doi.org/10.1080/00288330.2014.992918

De Boer, Agatha, M., Graham, R. M., Thomas, M. D., & Kohfeld, K. E. (2013). The control of the Southern Hemisphere Westerlies on the position of the Subtropical Front. *Journal of Geophysical Research: Oceans*, *118*, 5669–5675. https://doi.org/10.1002/jgrc.20407

Deacon, G. E. R. (1982). Physical and biological zonation in the Southern-Ocean. *Deep-Sea Research Part A-Oceanographic Research Papers*, *29*, 1–15.

Debreu, L., Vouland, C., & Blayo, E. (2008). AGRIF: Adaptive grid refinement in Fortran. *Computers & Geosciences*, *34*, 8–13.

Dong, Bo, & Dai, A. (2015). The influence of the interdecadal Pacific oscillation on temperature and precipitation over the globe. *Climate Dynamics*, *45*, 2667–2681.

Edwards, R. J., & Emery, W. J. (1982). Australasian Southern Ocean frontal stucture during summer 1976-77. *Marine and Freshwater Research*, *33*, 3–22.

Fernandez, D., Bowen, M., & Carter, L. (2014). Intensification and variability of the confluence of subtropical and subantarctic boundary currents east of New Zealand. *Journal of Geophysical Research: Oceans*, *119*, 1146–1160. https://doi.org/10.1002/2013JC009153

Good, S. A., Martin, M. J., & Rayner, N. A. (2013). EN4: Quality controlled ocean temperature and salinity profiles and monthly objective analyses with uncertainty estimates. *Journal of Geophysical Research: Oceans*, *118*, 6704–6716. https://doi.org/10.1002/2013JC009067

Graham, R. M., & De Boer, A. M. (2013). The dynamical subtropical front. *Journal of Geophysical Research: Oceans*, *118*, 5676–5685. https://doi.org/10.1002/jgrc.20408

Graham, R. M., de Boer, A. M., Heywood, K. J., Chapman, M. R., & Stevens, D. P. (2012). Southern ocean fronts: Controlled by wind or topography? *Journal of Geophysical Research*, *117*, C08018. https://doi.org/10.1029/2012JC007887

Gupta, S., Alex, S. McG., Sebille, E. V., Ganachaud, A., Brown, J. N., & Santoso, A. (2016). Future changes to the Indonesian Throughflow and Pacific circulation: The differing role of wind and deep circulation changes. *Geophysical Research Letters*, *43*, 1669–1678. https://doi.org/10.1002/2016GL067757

Hamilton, L. J. (2006). Structure of the subtropical front in the Tasman Sea. *Deep-Sea Research Part I-Oceanographic Research Papers*, *53*, 1989–2009.

Hansen, J., Ruedy, R., Sato, M., & Reynolds, R. (1996). Global surface air temperature in 1995: Return to pre-Pinatubo level. *Geophysical Research Letters*, *23*, 1665–1668. https://doi.org/10.1029/96GL01040

Hill, K. L., Rintoul, S. R., Coleman, R., & Ridgway, K. R. (2008). Wind forced low frequency variability of the East Australia Current. *Geophysical Research Letters*, *35*, L08602. https://doi.org/10.1029/2007GL032912

Hill, K. L., Rintoul, S. R., Oke, P. R., & Ridgway, K. (2010). Rapid response of the East Australian Current to remote wind forcing: The role of barotropic-baroclinic interactions. *Journal of Marine Research*, *68*, 413–431.

Hill, K. L., Rintoul, S. R., Ridgway, K. R., & Oke, P. R. (2011). Decadal changes in the South Pacific western boundary current system revealed in observations and ocean state estimates. *Journal of Geophysical Research*, *116*, C01009. https://doi.org/10.1029/2009JC005926

Hogg, A. McC., Meredith, M. P. D. P., Abrahamsen, E. P., Hughes, C. W., & Morrison, A. K. (2015). Recent trends in the Southern Ocean eddy field. *Journal of Geophysical Research: Oceans*, *120*, 257–267. https://doi.org/10.1002/2014JC010470

Holbrook, N. J., Goodwin, I. D., McGregor, S., Molina, E., & Power, S. B. (2011). ENSO to multi-decadal time scale changes in East Australian Current transports and Fort Denison sea level: Oceanic Rossby waves as the connecting mechanism. *Deep Sea Research Part II: Topical Studies in Oceanography*, *58*, 547–558.

Hu, D., Wu, L., Cai, W., Gupta, A. S., Ganachaud, A., Qiu, Bo, et al. (2015). Pacific western boundary currents and their roles in climate. *Nature*, *522*, 299–308.

Jeffrey, M. Z. (1986). *Climatological features of the subtropical convergence in Australian and New Zealand waters*, Sydney, Australia: Ocean Sciences Institute, University of Sydney.

Kerr, T. (2013). The contribution of snowmelt to the rivers of the South Island, New Zealand. *Journal of Hydrology (New Zealand)*, *52*, 61–82.

Kim, Y. S., & Orsi, A. H. (2014). On the variability of Antarctic circumpolar current fronts inferred from 1992–2011 altimetry'. *Journal of Physical Oceanography*, *44*, 3054–3071.

Kiss, A. E., Hogg, A. M., Hannah, N., Dias, F. B., Brassington, G. B., Chamberlain, M. A., et al. (2020). ACCESS-OM2 v1.0: a global ocean-sea ice model at three resolutions. *Geoscientific Model Development*, *13*, 401–442.

Li, Z. Y., Holbrook, N. J., Zhang, X. B., Oliver, E. C. J., & Cougnon, E. A. (2020). Remote Forcing of Tasman Sea Marine Heatwaves'. *Journal of Climate*, *33*, 5337–5354.

Mata, M. M., Tomczak, M., Wijffels, S., & Church, J. A. (2000). East Australian current volume transports at 30°S: Estimates from the World Ocean circulation experiment hydrographic sections PR11/P6 and the PCM3 current meter array. *Journal of Geophysical Research*, *105*, 28509–28526. https://doi.org/10.1029/1999JC000121

Meehl, G. A., Aixue Hu, B. D. S., & Xie, S.-P. (2016). Contribution of the Interdecadal Pacific Oscillation to twentieth-century global surface temperature trends. *Nature Climate Change*, *6*, 1005–1008.

Meijers, A. J. S. (2014). The Southern Ocean in the Coupled Model Intercomparison Project phase 5. *Philosophical transactions. Series A, Mathematical, physical, and engineering sciences*, *372*, 20130296.

Morris, M., Stanton, B., & Neil, H. (2001). Subantarctic oceanography around New Zealand: Preliminary results from an ongoing survey. *New Zealand Journal of Marine and Freshwater Research*, *35*, 499–519.

Munk, W. H. (1950). On the Wind-Driven Ocean Circulation. *Journal of Meteorology*, *7*, 79–93.

Oke, P. R., Pilo, G. S., Ridgway, K., Kiss, A., & Rykova, T. (2019). A search for the Tasman Front. *Journal of Marine Systems*, *199*.

Oke, P. R., Roughan, M., Cetina-Heredia, P., Pilo, G. S., Ridgway, K. R., Rykova, T., et al. (2019). Revisiting the circulation of the East Australian Current: Its path, separation, and eddy field. *Progress in Oceanography*, 176.

Oliver, E. C. J., & Holbrook, N. J. (2014). 'Extending our understanding of South Pacific gyre spin-up: Modeling the East Australian Current in a future climate. *Journal of Geophysical Research: Oceans*, *119*, 2788–2805. https://doi.org/10.1002/2013JC009591

Oliver, E. C. J., O'Kane, T. J., & Holbrook, N. J. (2015). Projected changes to Tasman Sea eddies in a future climate. *Journal of Geophysical Research-Oceans*, *120*, 7150–7165. https://doi.org/10.1002/2015JC010993

Orsi, A. H., Whitworth, T., & Nowlin, W. D. (1995). On the meridional extent and fronts of the Antarctic circumpolar current. *Deep-Sea Research Part I-Oceanographic Research Papers*, *42*, 641–673.

Parker, D. E., Wilson, H., Jones, P. D., Christy, J. R., & Folland, C. K. (1996). The impact of Mount Pinatubo on world-wide temperatures. *International Journal of Climatology*, *16*, 487–497.

Ridgway, K. R. (2007). Long-term trend and decadal variability of the southward penetration of the East Australian Current. *Geophysical Research Letters*, *34*, L13613. https://doi.org/10.1029/2007GL030393

Ridgway, K. R., Coleman, R. C., Bailey, R. J., & Sutton, P. (2008). Decadal variability of East Australian Current transport inferred from repeated high-density XBT transects, a CTD survey and satellite altimetry. *Journal of Geophysical Research*, *113*, C08039. https://doi.org/10.1029/2007JC004664

Ridgway, K. R., & Dunn, J. R. (2003). Mesoscale structure of the mean East Australian Current System and its relationship with topography. *Progress in Oceanography*, *56*, 189–222.

Rio, M. H., & Hernandez, F. (2004). A mean dynamic topography computed over the world ocean from altimetry, in situ measurements, and a geoid model. *Journal of Geophysical Research*, *109*, C12032. https://doi.org/10.1029/2003JC002226

Roemmich, D., Church, J., Gilson, J., Monselesan, D., Sutton, P., & Wijffels, S. (2015). Unabated planetary warming and its ocean structure since 2006. *Nature Climate Change*, *5*, 240–245.

Roemmich, D., & Gilson, J. (2009). 'The 2004–2008 mean and annual cycle of temperature, salinity, and steric height in the global ocean from the Argo Program. *Progress in Oceanography*, *82*, 81–100.

Roemmich, D., Gilson, J., Davis, R., Sutton, P., Wijffels, S., Riser, S., et al. (2007). Decadal Spinup of the South Pacific Subtropical Gyre. *Journal of Physical Oceanography*, *37*, 162–173.

Roemmich, D., Gilson, J., Sutton, P., & Zilberman, N. (2016). Multidecadal change of the south Pacific gyre circulation. *Journal of Physical Oceanography*, *46*, 1871–1883.

Roemmich, D., Gilson, J., Willis, J., Sutton, P., & Ridgway, K. (2005). Closing the time-varying mass and heat budgets for large ocean areas: The Tasman box. *Journal of Climate*, *18*, 2330–2343.

Salinger, M. J., Renwick, J. A., & Mullan, A. B. (2001). Interdecadal Pacific oscillation and south Pacific climate. *International Journal of Climatology*, *21*, 1705–1721.

Sallée, J. B., Speer, K., & Morrow, R. (2008). Response of the Antarctic circumpolar current to atmospheric variability. *Journal of Climate*, *21*, 3020–3039.

Sloyan, B. M., Ridgway, K. R., Cowley, R., & Bernadette, M. (2016). The East Australian Current and Property Transport at 27°S from 2012 to 2013. *Journal of Physical Oceanography*, *46*, 993–1008.

Smith, R. O., Vennell, R., Bostock, H. C., & Williams, M. J. M. (2013). Interaction of the subtropical front with topography around southern New Zealand. *Deep-Sea Research Part I-Oceanographic Research Papers*, *76*, 13–26.

Smythe-Wright, D., Chapman, P., Rae, C. D., Shannon, L. V., & Boswell, S. M. (1998). Characteristics of the South Atlantic subtropical frontal zone between 15 degrees W and 5 degrees E'. *Deep-Sea Research Part I-Oceanographic Research Papers*, *45*, 167–192.

Sokolov, S., & Rintoul, S. R. (2007). On the relationship between fronts of the Antarctic Circumpolar Current and surface chlorophyll concentrations in the Southern Ocean. *Journal of Geophysical Research-Oceans*, *112*(C7), C07030. https://doi.org/10.1029/2006JC004072

Sokolov, S., & Rintoul, S. R. (2009). Circumpolar structure and distribution of the Antarctic Circumpolar Current fronts: 1. Mean circumpolar paths. *Journal of Geophysical Research-Oceans*, *114*, C11018. https://doi.org/10.1029/2008JC005108

Sokolov, S., & Rintoul, S. R. (2009). Circumpolar structure and distribution of the Antarctic Circumpolar Current fronts: 2. Variability and relationship to sea surface height. *Journal of Geophysical Research-Oceans*, *114*, C11019. https://doi.org/10.1029/2008JC005248

Sokolov, S., & Rintoul, S. R. (2002). 'Structure of Southern Ocean fronts at 140 degrees E'. *Journal of Marine Systems*, *37*, 151–184.

Stanton, B. R. (2010). An oceanographic survey of the Tasman Front. *New Zealand Journal of Marine and Freshwater Research*, *15*, 289–297.

Storkey, D., Blaker, A. T., Mathiot, P., Megann, A., Aksenov, Y., Blockley, E. W., et al. (2018). UK Global Ocean GO6 and GO7: A traceable hierarchy of model resolutions. *Geoscientific Model Development*, *11*, 3187–3213.

Stramma, L. (1992). The South Indian-ocean current. *Journal of Physical Oceanography*, *22*, 421–430.

Stramma, L., Peterson, R. G., & Tomczak, M. (1995). The South Pacific current'. *Journal of Physical Oceanography*, *25*, 77–91.

Sutton, P. (2001). Detailed structure of the Subtropical Front over Chatham Rise, east of New Zealand. *Journal of Geophysical Research*, *106*, 31045. https://doi.org/10.1029/2000JC000562

Sutton, P. J. H., Bowen, M., & Dean, R. (2005). Decadal temperature changes in the Tasman Sea. *New Zealand Journal of Marine and Freshwater Research*, *39*, 1321–1329.

Sutton, P. J. H., & Chiswell, S. M. (1996). Effect of volcanic aerosols on satellite-derived sea surface temperatures around New Zealand. *New Zealand Journal of Marine and Freshwater Research*, *30*, 105–113.

Szymanska, K., & Tomczak, M. (1994). Subduction of central water near the subtropical front in the Southern Tasman sea. *Deep-Sea Research Part I-Oceanographic Research Papers*, *41*, 1373–1386.

Tilburg, C. E., Hurlburt, H. E., O'Brien, J. J., & Shriver, J. F. (2002). Remote topographic forcing of a baroclinic western boundary current: An explanation for the Southland Current and the pathway of the subtropical front east of New Zealand. *Journal of Physical Oceanography*, *32*, 3216–3232.

Tsujino, H., Urakawa, S., Nakano, H., Justin Small, R., Kim, W. M., Yeager, S. G., et al. (2018). JRA-55 based surface dataset for driving ocean–sea-ice models (JRA55-do). *Ocean Modelling*, *130*, 79–139.

Uddstrom, M. J., & Oien, N. A. (1999). On the use of high-resolution satellite data to describe the spatial and temporal variability of sea surface temperatures in the New Zealand region. *Journal of Geophysical Research-Oceans*, *104*, 20729–20751. https://doi.org/10.1029/1999JC900167

Williams, J., Morgenstern, O., Varma, V., Behrens, E., Hayek, W., Oliver, H., et al. (2016). Development of the New Zealand Earth System Model: NZESM. *Weather and Climate*, *36*, 25–44.

Yang, Hu, Lohmann, G., Krebs-Kanzow, U., Ionita, M., Shi, X., Sidorenko, D., et al. (2020). 'Poleward shift of the major ocean Gyres detected in a warming climate. *Geophysical Research Letters*, *47*, e2019GL085868. https://doi.org/10.1029/2019GL085868

Zilberman, N. V., Roemmich, D. H., Gille, S. T., Gilson, J., Zilberman, N. V., Roemmich, D. H., et al. (2018). Estimating the velocity and transport of western boundary current systems: A case study of the east Australian current near Brisbane. *Journal of Atmospheric and Oceanic Technology*, *35*, 1313–1329.